Coupled GCM Simulation of Atmosphere–Ocean Variability Associated with Zonally Asymmetric SST Changes in the Tropical Indian Ocean

Ngar-Cheung Lau and Mary Jo Nath

NOAA/Geophysical Fluid Dynamics Laboratory, Princeton University, Princeton, New Jersey

ABSTRACT

The nature of a recurrent pattern of variability in the tropical Indian Ocean (IO) during the boreal autumn has been investigated using a 900-yr experiment with a coupled atmosphere–ocean general circulation model. This Indian Ocean Pattern (IOP) is characterized by zonal surface wind perturbations along the equator, as well as east–west contrasts in the anomalous sea surface temperature (SST), surface pressure, and precipitation fields. The IOP is seen to be linked to the El Niño–Southern Oscillation (ENSO) phenomenon in the tropical Pacific. By constructing composite charts and analyzing the heat budget for the top ocean layer, it is illustrated that the ENSO-related changes in the surface wind modify the intensity of oceanic upwelling, horizontal temperature advection, and surface heat fluxes in various parts of the IO basin. These processes lead to SST perturbations with opposite signs in the eastern and western equatorial IO.

Further diagnosis of the model output reveals that some strong IOP episodes occur even in the near absence of ENSO influences. In such IOP events that do not coincide with prominent ENSO development, the most noteworthy signal is a zonally elongated sea level pressure anomaly situated south of Australia during the southern winter. The anomalous atmospheric circulation on the equatorward flank of this feature contributes to the initiation of IOP-like events when the ENSO forcing is weak. Both simulated and observational data show that the pressure anomaly south of Australia is part of a hemisphere-wide pattern bearing a considerable resemblance to the Antarctic Oscillation. This annular mode of variability is characterized by opposite pressure changes in the midlatitude and polar zones, and is only weakly correlated with ENSO.

The findings reported here indicate that the IOP is attributable to multiple factors, including remote influences due to ENSO and extratropical changes, as well as internal air–sea feedbacks occurring within the IO basin.

---

1. Introduction

In view of the proximity of the Indian Ocean (IO) to some of the most densely populated regions of the world, the impacts of atmosphere–ocean variability in this basin on the weather and climate of the surrounding areas have received considerable attention from the research community. For instance, the role of sea surface temperature (SST) anomalies at various IO sites in the variability of the Indian summer monsoon has been investigated by Weare (1979), Hastenrath et al. (1993), Shukla (1987), and Nicholls (1995), among many others. Interest in the interannual variability in the IO sector was further heightened by the prominent climatic events that occurred in 1997–98 (e.g., see Webster et al. 1999; Chambers et al. 1999). During the northern autumn season of 1997, below-normal SST, convective activity, and sea level prevailed over the eastern equatorial IO, whereas positive SST, precipitation, and sea level anomalies were observed over the western portion of this

basin. These signals were accompanied by strong easterly surface wind anomalies along the equator in autumn. Analysis of the observational records for the past 40 yr by Saji et al. (1999) indicates that the atmospheric and oceanic changes during several other events in this period exhibit similar characteristics as those seen in 1997–98. To emphasize the opposite SST anomalies appearing in the eastern and western parts of the IO basin, these authors referred to this recurrent pattern of variability as a "dipole mode." Both Webster et al. (1999) and Saji et al. (1999) also proposed that this mode is primarily a manifestation of local atmosphere–ocean interactions confined to the IO basin, and that remote influences play a less significant role.

In recent years, the phenomena and processes related to the characteristic IO pattern described above have been the focus of many investigations. The structure of, and relationships between, various atmospheric and oceanic changes associated with this pattern have been described by Yu and Rienecker (1999), Saji and Yamagata (2003), Rao et al. (2002), and Xie et al. (2002) using observational data. Simulations of different aspects of such phenomenon have been made using models of varying degrees of complexity, including a 2.5-layer

Corresponding author address: Dr. Ngar-Cheung Lau, NOAA/ Geophysical Fluid Dynamics Laboratory, Princeton University, P.O. Box 308, Princeton, NJ 08542.
E-mail: Gabriel.Lau@noaa.gov

thermodynamic ocean model (Behera et al. 1999), a reduced gravity primitive equation model of the IO basin (Murtugudde et al. 2000), general circulation models (GCMs) of the global ocean (Vinayachandran et al. 2002; Li et al. 2002), and coupled atmosphere–ocean GCMs (Iizuka et al. 2000; Loschnigg et al. 2003).

Concurrent with these research efforts is a vigorous debate within the community concerning the physical reality of the dipole mode in the IO. Some of the contrasting viewpoints on this and other issues are summarized in the correspondence between Allan et al. (2001) and Yamagata et al. (2002). In particular, Dommenget and Latif (2002, 2003) documented cases in which dipole-like patterns are obtained in an unrotated empirical orthogonal function (EOF) analysis, but not in rotated EOF and simple regression analyses, thus suggesting that the dipole structure could be an artifact of the specific analysis method being used, and may not necessarily correspond to physically meaningful modes. Hastenrath (2002) further pointed out that the IO pattern should be interpreted in terms of changes in the zonal SST gradient, instead of an east–west SST seesaw. On the other hand, Behera et al. (2003) presented a counter example in which a monopole mode and a dipole mode have both been intentionally prescribed in a synthetic dataset. These investigators demonstrated that the rotated EOF and simple regression approaches failed to retrieve the dipole mode, and hence argued that the results from these methods could at times be misleading. In view of the controversial nature of labels such as "dipole" or "zonal mode," we shall henceforth refer to the recurrent SST anomaly with east–west contrast as the Indian Ocean Pattern (IOP), which avoids conveyance of any particular notion of the physical nature of this phenomenon.

Another point of contention among various investigators is the degree of dependency of the IOP on El Niño–Southern Oscillation (ENSO) processes in the tropical Pacific. Saji et al. (1999) reported a weak simultaneous correlation (<0.35) between indices of ENSO and the IOP when all months of the year are taken into account, and concluded that these two modes of variability are independent of each other. However, Allan et al. (2001), Huang and Kinter (2002), Krishnamurthy and Kirtman (2003), and Shinoda et al. (2004, hereafter SAH) noted that this correlation increases to 0.56–0.75 when only the mean September–October–November (SON) data are used in the computation. Some of these authors also stressed the importance of considering the temporal lead/lag relationships between various characteristic patterns within the IO, and the seasonal dependence of linkages between such patterns and ENSO. Furthermore, global composite charts have been presented by Reason et al. (2000) on the basis of major ENSO episodes in the 1877–1993 period. Their results indicate that such occurrences are accompanied by significant SST, cloudiness, and surface wind anomalies in the IO sector during the October–November–December

(OND) season, with spatial patterns that are similar to those associated with recent IOP events. The higher level of correlation between the IOP and ENSO for seasonally stratified data, as well as the possibility of interactions between Pacific and IO phenomena on some occasions, were recognized by Yamagata et al. (2002). Rao et al. (2002) and Saji and Yamagata (2003) estimated that about one-third of the IOP episodes in the observational record occurred at the same time as ENSO events. However, these authors also noted that a considerable fraction of the IOP cases were not accompanied by ENSO, and, conversely, many ENSO events took place without prominent IOP signals. They hence maintained that IOP could still exist in the absence of remote forcing from ENSO.

The identification of temporal relationships between IOP and ENSO is further complicated by the multiple time scales inherent in ENSO variability. Observational evidence presented by Enfield and Mestas-Nuñez (1999), Tourre et al. (2001), and White and Allan (2001) indicates that the climate system exhibits ENSO-like characteristics on a broad range of frequency bands, including the quasi-biennial, multiyear, and decadal periods. Allan et al. (2003) pointed out that modulations by the decadal scale could result in "protracted" ENSO episodes. Even if an overall relationship exists between the protracted ENSO episode and the IOP on decadal time scales, such a correspondence would not be apparent in those stages of the episode when the ENSO signal associated with a particular (e.g., quasi biennial) time scale happens to be opposite to the corresponding signal associated with another (e.g., interannual) time scale. The latter phase interactions yield a weak net ENSO forcing, whereas the IOP signature remains strong due to decadal modulations. Such circumstances would therefore give the impression that IOP could occur when there is apparently no ENSO influence from the Pacific.

The processes contributing to covariability between the IO and Pacific basins, as noted in the preceding paragraphs, have been the subject of many recent studies. Kawamura (1998), Klein et al. (1999), and Wang et al. (2004) presented observational evidence on the crucial role of the atmospheric circulation in linking SST changes in the Pacific to those in the IO. In essence, this tropical "atmospheric bridge" mechanism operates in the following manner: during an ENSO event, the anomalous SST forcing in the Pacific sector generates an atmospheric response that extends toward the IO basin; such atmospheric perturbations in turn alter the surface conditions of the IO through changes in the heat and momentum fluxes at the air–sea interface. The relevance of this chain of processes to the interactions between the Pacific and IO basins has been demonstrated in the numerical simulations analyzed by Baquero-Bernal et al. (2002), Lau and Nath (2003), and SAH. The experimental design for these model studies typically entails the inclusion of ENSO variability in the

Pacific sector (as produced by a coupled GCM or as prescribed using temporally evolving SST observations), and detection of the ensuing atmosphere–ocean responses in the IO basin.

The primary goal of the present study is to further investigate the nature of the IOP—its spatiotemporal characteristics, its relationships with ENSO as well as other modes of variability, and the role of various atmospheric and oceanic processes in individual stages of its life cycle. Our modeling effort is aimed at addressing some of the scientific issues concerning the physical nature of the IOP and the degree of dependence of this phenomenon on ENSO. This work is part of an ongoing effort [see recent review by Alexander et al. (2002)] to examine the origin of coupled variability in different parts of the World Ocean by using model tools developed at the Geophysical Fluid Dynamics Laboratory (GFDL). In this series of experiments, the air–sea interaction in the ocean basin of interest has thus far been studied by evaluating the impact of surface fluxes on a motionless oceanic mixed layer model. This model framework yields no information on the contributions of transport processes within the ocean. The observational and model results reviewed earlier in this section indicate that the occurrence of IOPs is accompanied by notable changes in the oceanic circulation. In order to incorporate the effects of both ocean dynamics and surface fluxes on IO variability, we have chosen to conduct this study on the basis of a 900-yr integration of a fully coupled atmosphere–ocean GCM. The duration of this experiment, which is considerably longer than those analyzed by other authors in the published literature, provides an adequate sampling of various classes of IOP events that are linked to different causes.

The model and observational tools used in this study are described in section 2. The spatial structure of the simulated modes of SST variability in the IO and tropical Pacific basins are documented in section 3. The temporal evolution of IOP events that occur in conjunction with ENSO and the local oceanic heat budget during such events, are examined in sections 4 and 5, respectively. The nature of those IOP events that are not accompanied by strong ENSO development is investigated in section 6. The relationships among the modes of variability considered in this study are evaluated in section 7.

2. Description of model experiment and observational datasets

The basic model tool for this study is the coupled atmosphere–ocean GCM developed by the Climate Dynamics Project at GFDL. A detailed account of the model structure, integration procedure, and performance has been given by Delworth et al. (2002), who have named the experiment to be analyzed here as CONTROL_C.

The atmospheric component of this model is almost identical to that used in recent works on the relationships between ENSO and interannual changes in the climate of the Indo-Pacific basin (Lau and Nath 2000, 2003; SAH). Meteorological fields are represented using a spectral formulation with rhomboidal truncation at 30 zonal wavenumbers, and a transform grid with grid spacings of ~2.2° latitude × 3.75° longitude. Vertical variations are computed at 14 sigma levels.

The oceanic component of the coupled GCM corresponds to version 1.1 of the Modular Ocean Model, as documented in Pacanowski et al. (1991). The meridional structure of the oceanic grid matches exactly with that of the atmospheric transform grid. In the zonal direction, two oceanic grid boxes are placed under each atmospheric grid box, so that the longitudinal spacing between adjacent ocean grid points is 1.875°. There are altogether 18 vertical oceanic levels, with the top layer having a thickness of 40 m.

In order to minimize the climate drifts of the coupled model system resulting from imbalances between its atmospheric and oceanic components, a flux adjustment technique has been employed for the initialization and integration of this model [see description of the CONTROL_C run in Delworth et al. (2002)]. This procedure leads to a stable integration with only minor long-term trends in various global measures of temperature, salinity, and sea ice. In the course of the 900-yr experiment, exchanges of heat, water, and momentum across the atmosphere–ocean interface were made once per day.

Some of the model results in our study have been compared with the corresponding statistics based on observations. The latter datasets include the SST analyses produced by Smith et al. (1996) using EOF reconstruction, and selected atmospheric fields produced by the National Centers for Environmental Prediction–National Center for Atmospheric Research (NCEP–NCAR) reanalysis project (Kalnay et al. 1996). Both of these SST and NCEP–NCAR data archives cover the period of 1950–99. In order to focus on the variability on interannual time scales, linear trends have been subtracted from both the model and observational data prior to the diagnoses presented in the following sections.

3. Identification of prominent IOP and ENSO episodes

The atmospheric and oceanic signals associated with the life cycles of IOP and ENSO are characterized by complex spatiotemporal development. Application of pattern recognition techniques (e.g., lagged correlation analysis, EOF analysis and its variants, etc.) to observational datasets indicates that two or more modes or indices may be needed to fully capture the richness of the IOP or ENSO features (e.g., Tourre and White 1995, 1997; Trenberth and Stepaniak 2001). The suitability of some of the commonly used indices for representing ENSO has been evaluated by Hanley et al. (2003). A comprehensive search of the optimal analysis approach for portraying the typical evolution of IOP and ENSO

events is beyond the scope of the present study. We shall instead confine our attention in this section to the identification of high-amplitude IOP and ENSO episodes on the basis of simple areal averages of SST over appropriate sites selected in previous studies. The relationships between the anomalous episodes occurring in the IO and Pacific basins, as well as their space–time behavior will then be documented in the following section using correlation statistics and composite charts.

a. Indian Ocean basin

Following the methodology of Saji et al. (1999) and Baquero-Bernal et al. (2002), two indices have been constructed on the basis of normalized SST anomalies averaged over the southeastern tropical Indian Ocean (SETIO) and the western tropical Indian Ocean (WTIO) separately. For the model data, these two sites are defined as the oceanic grid points in the IO sector of the regions (10°S–0°, 90°–110°E) and (10°S–10°N, 40°–60°E), respectively. For the observations, the corresponding sites are (10°S–0°, 90°–110°E) and (10°S–10°N, 50°–70°E), respectively, and are identical to those used by Saji et al. (1999). As will be seen presently, the slight westward shift of the WTIO site for the model data relative to that for the observations accommodates a corresponding spatial displacement between the simulated and observed features in that region.

The regression coefficients of SST anomalies at individual grid points versus the indices as defined above are displayed in Fig. 1, for the 900-yr model dataset (left panels) and the 50-yr observational dataset (right panels), and for regressions upon the WTIO index (upper panels), the SETIO index with reversed sign (middle panels), and WTIO minus SETIO (lower panels). All computations are based on averages over the northern autumn season (SON). Both model and observational results are indicative of a negative correlation between SST fluctuations off the coasts of Sumatra–Java and those in the western equatorial IO. The strongest SST anomalies in the western IO are simulated along the east African coast, whereas the corresponding observed feature is centered at ~60°E. This discrepancy has been taken into account in the different definitions of the WTIO region for the model and observational data. When compared with the observations, the simulated SST anomaly in the eastern equatorial IO has a relatively higher amplitude, and extends farther toward the central portion of the basin. We shall henceforth refer to the difference between the standardized SST anomalies at the WTIO and SETIO regions as the IOP index.

The seasonal dependence of the level of anticorrelation between simulated SST anomalies in the western and eastern IO has been examined by computing separately the correlation coefficients between the WTIO and SETIO indices defined for each of the 12 calendar months. It is seen that anticorrelations between these indices are simulated in the July–December period, with highest negative values in August (−0.34), September (−0.42), and October (−0.40). The correlations are weakly positive in the January–May period. These results indicate that the IOP in the model is strongest during the northern late summer and fall seasons.

b. Pacific basin

Knutson and Manabe (1998) have analyzed the characteristics of ENSO-like events appearing in an experiment based on a coupled GCM similar to that used in the present study. They reported that the evolution of the oceanic heat content during such events is reminiscent of the behavior of the delayed oscillator mode (Schopf and Suarez 1988). The composite SST pattern of the simulated ENSO events (see Fig. 4f of Knutson and Manabe 1998) is characterized by a zonally elongated extremum along the equatorial Pacific, with amplitudes peaking near the date line. We have accordingly constructed a temporal index for this pattern by averaging the SST anomalies over the site (5°S–5°N, 160°E–150°W), which is referred to as the Niño-4 region in the ENSO literature. The regression chart of the model SST field versus the standardized Niño-4 index for the SON season is shown in Fig. 2.

The simulated distribution in Fig. 2 may be compared with the typical SST patterns associated with observed ENSO events (e.g., see Fig. 1b of Lau and Nath 1996). The magnitude of the model SST anomaly is largest in the Niño-4 region. In contrast, the SST changes accompanying observed ENSO episodes are strongest between the date line and the South American coast. Hence we shall use the SST anomaly averaged over the region (5°S–5°N, 150°–90°W, often referred to as Niño-3) as an indicator of the observed ENSO variability. As has been noted by Knutson and Manabe (1998), the westward displacement of the model SST anomaly center relative to the observed position could be related to deficiencies in simulating the climatological SST and thermocline patterns in the equatorial Pacific. In particular, the cold tongue in this model extends too far to the central Pacific, so that the strongest zonal SST gradients are also dislocated toward the western Pacific.

4. Atmosphere–ocean changes in the IO basin accompanying ENSO events

a. Covariability between the IOP and ENSO

The relationship between the IOP and ENSO events may be portrayed by plotting representative indices of these two phenomena for individual years against each other. In the scatter diagram shown in Fig. 3a, the data for each SON season in the 900-yr experiment are indicated by a dot, with abscissa and ordinate corresponding to the standardized Niño-4 and IOP indices (see definitions in section 3) respectively. The model data are to be compared with Fig. 3b, where the observed
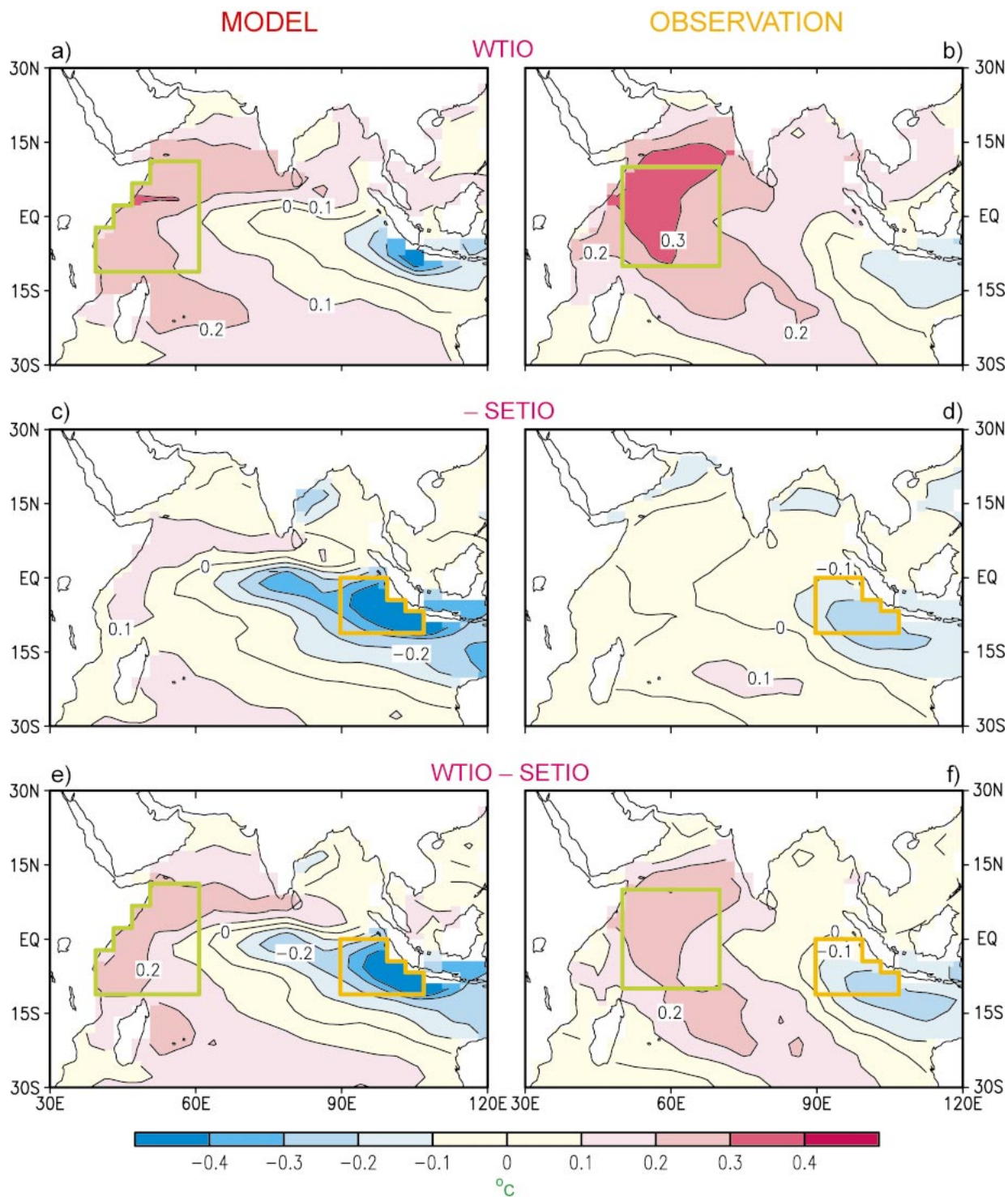
FIG. 1. Distributions of the regression coefficients of the SST field vs the indices for (a) and (b) WTIO, (c) and (d) SETIO with reversed polarity, and (e) and (f) WTIO minus SETIO, as computed using data from the (left) 900-yr model experiment and (right) 50-yr observations for the SON season. The indices represent standardized areal averages of SST data in the western and southeastern tropical IO, as indicated, respectively, by the green and orange frames in the appropriate panels. Contour interval: 0.1°C.
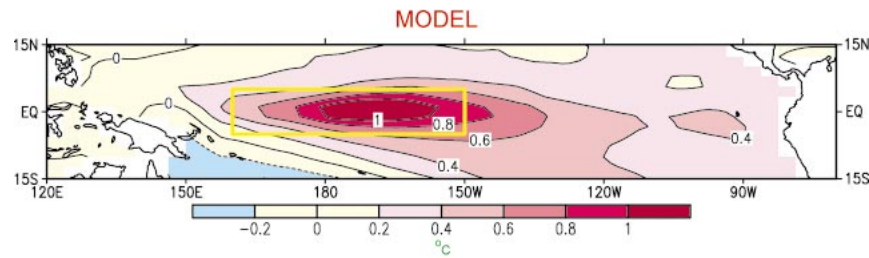
FIG. 2. Distribution of the regression coefficients of the SST field vs the Niño-4 index, as computed using data from the coupled model experiment for the SON season. The Niño-4 index corresponds to standardized areal average of SST values in the western and central equatorial Pacific (indicated by yellow rectangular frame). Contour interval: 0.2°C.

Niño-3 and IOP indices for individual boreal autumns in the 1950–99 period are displayed in an analogous manner. It is evident from Fig. 3 that the IOP and ENSO indices displayed in both panels exhibit rather strong correlations, with coefficients reaching 0.55 and 0.61 for the model and observations, respectively.[1]

In this section, we shall focus our attention on two groups of events in the model experiment. The first group (hereafter referred to as the high/warm set) consists of those autumns with high IOP indices exceeding $+1\sigma$, and with Niño-4 indices in the warm ranges between $+1\sigma$ and $+2\sigma$. The second group (the low/cold set) is composed of cases characterized by IOP and Niño-4 indices with low values less than -1σ and in the cold ranges of -1σ to -2σ, respectively. The 38 and 47 seasons that satisfy the criteria for the high/warm and low/cold sets are indicated in Fig. 3a using red and blue dots, respectively. In the following sections, averages of selected fields will be computed separately over these two groups of events. The differences between the composites (high/warm minus low/cold) will then be used to highlight the linear aspects of those strong IOP events that occur in conjunction with prominent ENSO episodes.[2]

Contrary to the results presented here, Iizuka et al. (2000) reported that the simulation based on another coupled GCM exhibits a much weaker linkage between

IOP and ENSO. Further investigations are needed to fully discern the impact of numerical formulations and physical parameterizations in different models on the degree of covariability between the IOP and ENSO phenomena.

b. Composite patterns of atmospheric and SST anomalies

The typical evolution near the air–sea interface when high-amplitude IOP and ENSO events take place simultaneously is portrayed in Fig. 4, which shows the high/warm minus low/cold composites of (top row) surface wind vector and wind speed, (middle row) sea level pressure and precipitation, and (bottom row) SST. Results are displayed for the June–July–August (JJA) (left panels) and SON (right panels) seasons. The polarity of the anomalies described in the following discussion pertains to the events in the high/warm composite. Features in the low/cold group would have the opposite polarity. By applying a two-tailed Student's t test to the composite patterns in Fig. 4, it is found that all the principal anomaly features described below are significant at the 99% level.

1) JJA SEASON

The near-equatorial precipitation pattern (shading in Fig. 4b) is dominated by an elongated positive center near the date line, and a dry belt extending across the Indonesian Archipelago. Below-normal precipitation prevails over the eastern and central equatorial IO, the southern IO, the northern two-thirds of the Indian subcontinent, and the South China Sea. The sea level pressure field (contours in Fig. 4b) is characterized by positive anomalies over the entire IO basin, with extrema over the southern IO and southern Australia. Negative pressure departures are simulated over the South Pacific east of the date line, and the subtropical northwestern Pacific. The near-surface equatorial circulation anomalies (arrows in Fig. 4a) are characterized by divergence from the dry zone in Indonesia, with anomalous easterlies over the IO, and westerlies over the western Pacific. The orientation of the anomalous wind vectors

---

[1] The spectra for the simulated and observed ENSO indices (see Fig. 11 of Delworth et al. 2002) suggest that the typical period of an ENSO "cycle" in the simulated (observed) system is approximately 8 (4) yr. Considering that there are 2 degrees of freedom in each ENSO cycle (consisting of a warm and a cold event), we assume that 4 (2) yr of model (observational) data are required to yield 1 degree of freedom. By applying a two-tailed Student's t test with this assumption, the threshold value for the correlation coefficient at the 95 (99)% significance level is estimated to be 0.13 (0.17) for the 900-yr model dataset, and 0.39 (0.51) for the 50-yr observational dataset.

[2] Figure 3a shows a skewed distribution of the ENSO episodes, that is, there are many warm ENSO events with Niño-4 $> +2\sigma$, but no cold events with Niño-4 $< -2\sigma$. To ensure that the ENSO events of comparable amplitudes are incorporated in the high/warm and low/cold composites, those extremely warm ($> +2\sigma$) cases have not been included in the high/warm group. Composites of the episodes with Niño-4 $> +2\sigma$ and IOP index $> +1\sigma$ (not shown) is qualitatively similar to the results based on the high/warm group, albeit with higher amplitudes in some instances.
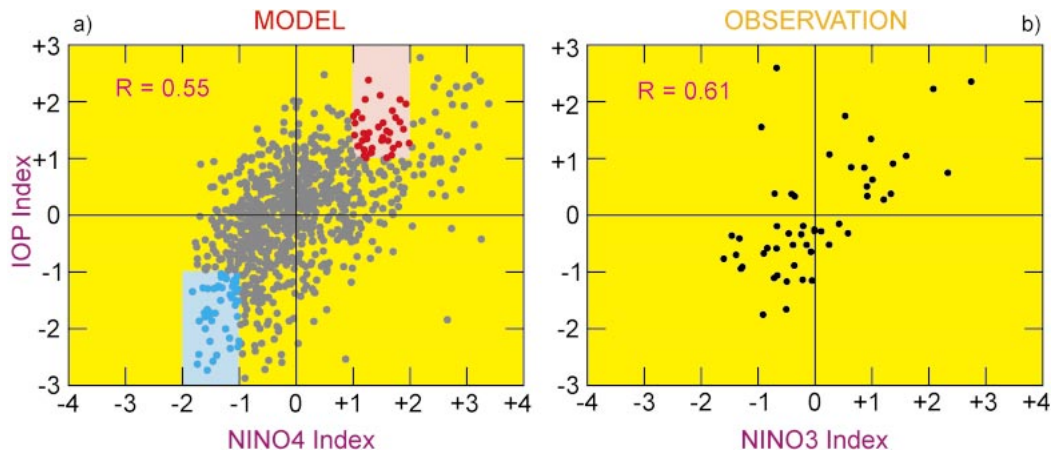
FIG. 3. Scatterplots of (a) IOP index vs Niño-4 index for the 900-yr model dataset and (b) IOP index vs Niño-3 index for the 50-yr observations. The abscissa (ordinate) of each dot in these diagrams represent the amplitude and sign of the Niño-3/Niño-4 (IOP) indices for an individual SON season. (a) Red and blue dots indicate the cases selected for constructing the high IOP/warm ENSO and low IOP/cold ENSO composites, respectively. The correlation coefficient between the pair of indices considered in each panel is displayed in the top-left corner of that panel.

over the equatorial eastern and central IO is parallel to that of the local time-mean circulation (see Figs. 1c and 1d of Lau and Nath 2000), thus resulting in above-normal wind speeds (shading in Fig. 4a) in that region. On the other hand, the anomalous westerlies over the equatorial western Pacific are directed against the climatological flow, thereby reducing the local wind speeds. The northeasterly anomaly and below-normal wind speeds off the Somali coast are indicative of a weakened summer monsoon circulation in that region. A broad anticyclonic flow pattern prevails over the southern IO and southern Australia. The SST pattern (Fig. 4c) shows a strong positive Pacific anomaly centered at the equator and east of the date line. Cold anomalies are discernible to the southwest and northwest of this center. In the IO sector, cold anomalies appear off the west and south coasts of the Indonesian Archipelago; whereas warming occurs along much of the eastern African seaboard, the Arabian Sea and east of Madagascar.

2) SON SEASON

The primary positive precipitation center over the western Pacific in this season (shading in Fig. 4e) is located west of its JJA position; whereas the centroid of the dry Indonesian anomaly is displaced southward. The contrast between the dry and wet conditions over the eastern and western tropical IO, respectively, is more apparent in SON than in JJA. The strongest positive sea level pressure anomaly (contours in Fig. 4e) is coincident with the dry anomaly center over northeastern Australia. The strengthened zonal pressure gradient across the southern tropical IO is accompanied by relatively more intense easterly anomalies and positive wind speed changes in that region (Fig. 4d). The anomalous SST pattern (Fig. 4f) in the tropical IO exhibits a stronger

east–west contrast than in JJA. These simulated atmospheric and SST changes bear considerable resemblance to the corresponding features observed during the mature phase of ENSO events in the tropical western Pacific (e.g., see Wallace et al. 1998), and IOP events in the IO basin (Webster et al. 1999; Saji et al. 1999).

It is evident from Fig. 4 that a strong correspondence exists among the surface wind anomalies in the central equatorial IO and the zonal contrasts of SST, surface pressure, and precipitation across the IO basin. The relationships between these individual facets of the IOP, as well as their covariability with ENSO, may be further illustrated by computing temporal correlations between representative indices of various features. For this purpose, the following indicators of atmosphere–ocean variability in the SON season are defined:

- U, the surface zonal wind averaged over the central tropical Indian Ocean (CTIO; 5°S–5°N, 70°–90°E); and
- ΔSST, ΔP, ΔR, as computed by subtracting the normalized areal averages of the SST, sea level pressure, and rainfall, respectively, over the SETIO region from the corresponding averages over the WTIO region.

The correlations among these four indices, as well as those between Niño-4 and the individual indices, are displayed in Table 1. The high correlation values in the first three columns of this table confirm the strong linkages between the surface wind, SST, pressure, and precipitation fields within the IO basin. Particularly strong correlations are seen between U and each of the east–west differences (ΔSST, ΔP, ΔR, see first three entries in first row of Table 1), thus indicating that the surface zonal wind over CTIO offers the most effective representation of the atmosphere–ocean variability associated with IOP. The correlations among the four indices
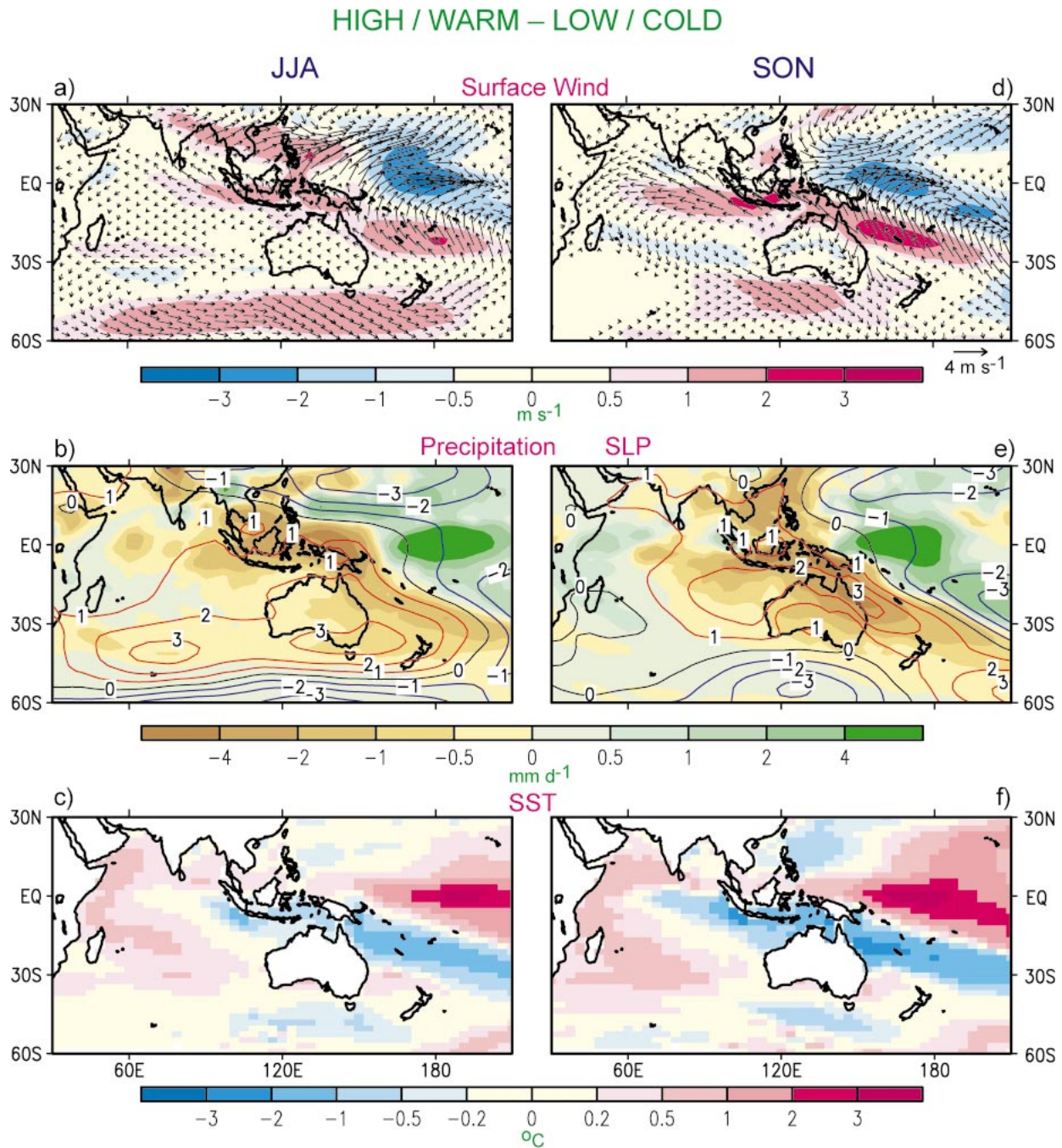
FIG. 4. Distributions of the high/warm minus low/cold composites of the (a) and (d) surface wind vector [arrows, see scale below (d)] and wind speed (shading), (b) and (e) sea level pressure (contours, interval: 1 mb) and precipitation (shading), and (c) and (f) SST. Results are based on model data for the (left) JJA and (right) SON seasons. The convention for the color shading in each pair of panels is depicted by a horizontal scale bar at the bottom of these panels.

defined for the IO basin are mostly higher than those between Niño-4 and each of these indices (see last column of Table 1). Of the four indices defined for the IO basin, Niño-4 exhibits the strongest correlation with ΔSST, thus offering further justification for the joint use of these two indices for constructing the composite charts in this study. Some of the results presented in

Table 1 may be compared with their observational counterparts as reported by Hastenrath et al. (1993), Behera and Yamagata (2003), and Saji and Yamagata (2003). The latter studies are in support of the central role of U in describing the atmospheric and oceanic anomalies accompanying IOP episodes. They also report a generally higher level of correlation among U, ΔSST, and

	ΔSST	ΔP	ΔR	Niño-4
U	−0.65	0.80	−0.69	−0.48
ΔSST		−0.67	0.50	0.55
ΔP			−0.63	−0.31
ΔR				0.24

ΔP, as compared to that between ENSO and these individual IO indices.

5. Heat budget of the top ocean layer during strong IOP/ENSO events

We proceed to study the implications of the atmospheric anomalies described in the previous section on the advective processes in the underlying ocean as well as energy fluxes across the air–sea interface. The contributions of these individual mechanisms to the establishment and sustenance of the SST anomaly pattern associated with the IOP may be assessed by evaluating the relevant terms in the balance equation for the anomalous temperature of the top ocean layer T':

$$\frac{\partial}{\partial t}T' = -(\mathbf{V}\cdot\nabla T)' - (wS)'$$

$$+ \frac{1}{\rho C_p H}(Q_{\text{SW}} + Q_{\text{LW}} + Q_{\text{LH}} + Q_{\text{SH}})', \quad (1)$$

where the prime represents departure from the time average; $\mathbf{V}$ and w the horizontal and vertical components of the current velocity in the top model ocean layer, respectively; $S = \partial T/\partial z$ the vertical temperature stratification; ρ and C_p the density and specific heat of ocean water, respectively; H the thickness of the top ocean layer (40 m); Q_{SW} and Q_{LW} the shortwave and longwave components of the radiative flux at the ocean surface, respectively; and Q_{LH} and Q_{SH} the surface latent and sensible heat fluxes, respectively. Positive (negative) values of the radiative and heat fluxes correspond to warming (cooling) of the surface oceanic layer. The effects of processes such as convective mixing and diffusion are not considered in the present analysis.

a. Spatial distributions of temperature advection and surface fluxes

In order to diagnose various facets of temperature advection the first two terms on the right-hand side of Eq. (1) may be linearized as $-\mathbf{V}'\cdot\nabla\overline{T} - \overline{\mathbf{V}}\cdot\nabla T' - w'\overline{S} - \overline{w}S'$, where the overbar denotes the time average. The terms $-\mathbf{V}'\cdot\nabla\overline{T}$ and $-w'\overline{S}$ represent the action of the anomalous currents on the time-mean temperature field; whereas $-\overline{\mathbf{V}}\cdot\nabla T'$ and $-\overline{w}S'$ indicate the effect of time-mean currents on the temperature anomaly. The spatial distributions of the four linearized temperature advection terms for the JAS period are displayed in the right panels of Fig. 5. In computing these terms, the high/warm minus low/cold composites (see section 4a) have been used for the quantities $\mathbf{V}'$, w', and T'; whereas the climatological means have been used for $\overline{\mathbf{V}}$, $\overline{w}$, and $\overline{T}$. The choice of the JAS season is predicated on the fact that these advective terms attain maximum amplitude during this phase of the evolution of the IOP (see following subsection). To facilitate the interpretation of the results in Figs. 5e–h, the distributions of the relevant mean or anomalous component of the velocity and temperature fields are shown to the left of each of the panels for the four advection terms. The patterns displayed in the left panels are $\mathbf{V}'$ and $\overline{T}$ (Fig. 5a), $\overline{\mathbf{V}}$ and T' (Fig. 5b), w' and $\overline{S}$ (Fig. 5c), and $\overline{w}$ and S' (Fig. 5d).

Inspection of the right panels of Fig. 5 reveals that the most important advective processes in the eastern tropical IO are associated with the terms $-w'\overline{S}$ (Fig. 5g) and $-\overline{\mathbf{V}}\cdot\nabla T'$ (Fig. 5f). The cooling tendency due to $-w'\overline{S}$ along the equatorial IO between 60°E and the Indonesian coasts is primarily caused by the collocation of anomalous equatorial and coastal upwelling with strong time-mean temperature stratification (Fig. 5c). The upwelling in this region is linked to anomalous easterly surface wind in the open ocean, as well as southeasterly (along shore) wind anomalies off the coasts of Sumatra and Java (Figs. 4a and 4d). In describing the IOP in section 3 (see Fig. 1), it has been noted that the simulated SST anomaly in SETIO and CTIO is too strong and extends too far westward when compared with observations. The considerable resemblance between the pattern of $-w'\overline{S}$ (Fig. 5g) and the SST regression charts (left panels of Fig. 1) in this region suggests that the difference between the simulated and observed IOP may be linked to the excessive influence of upwelling on the surface heat budget of the model ocean. The negative temperature changes produced by $-\overline{\mathbf{V}}\cdot\nabla T'$ within the 0°–15°S zone may be attributed to the action of the time-averaged current on the anomalous temperature gradient in the southern tropical IO (Fig. 5b).

In the western IO the anomalous surface current is oriented from the central equatorial IO to the relatively cooler waters along the Somali coast as well as the southern tropical IO (Fig. 5a), thus leading to warm advection in those regions (Fig. 5e). The prevalent anomalous northeasterly wind stress (Figs. 4a and 4d) over the western IO basin is accompanied by reduced upwelling and positive temperature tendencies immediately off the Somali coast (Figs. 5c and 5g). This effect
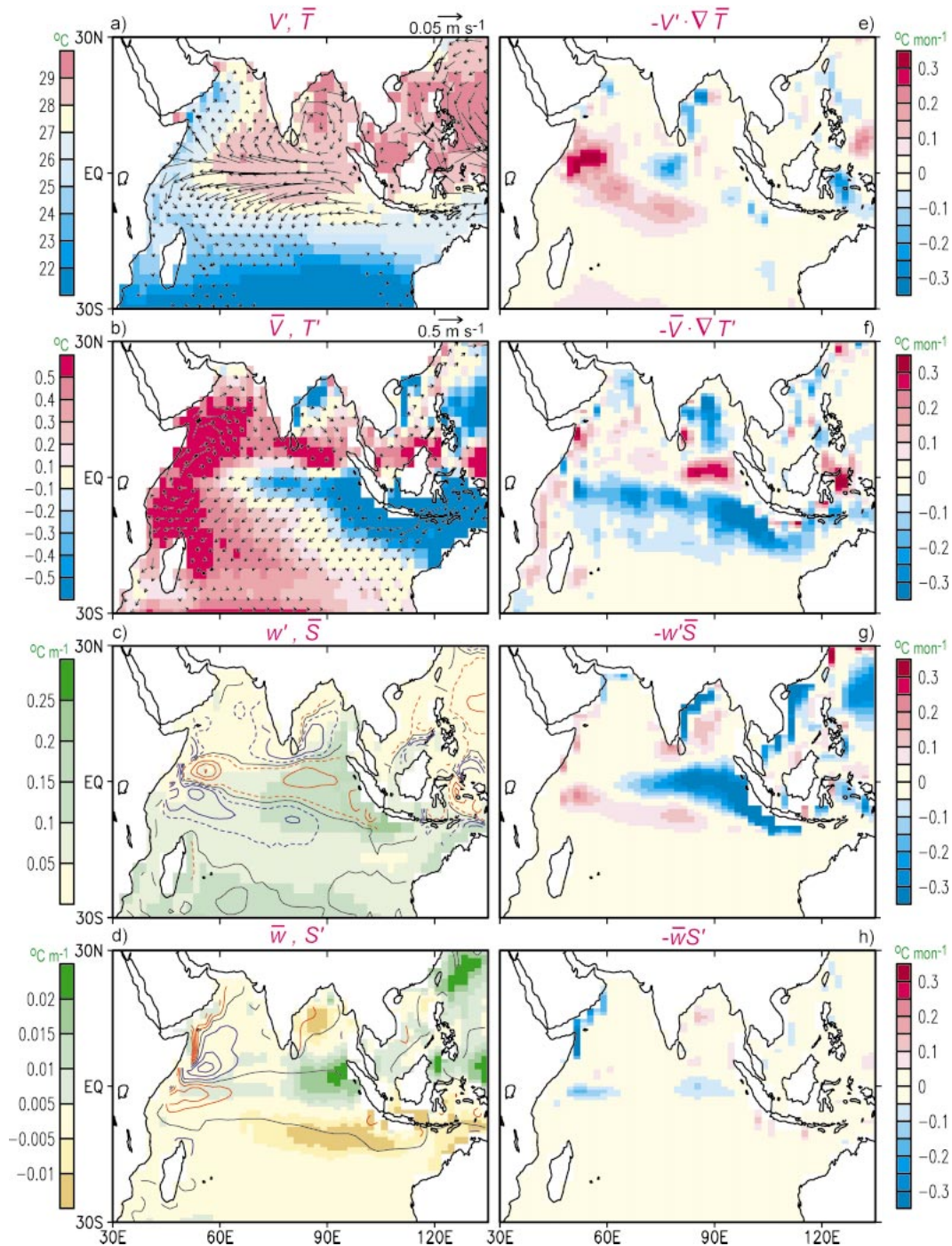
FIG. 5. Distributions of the (a) anomalous horizontal ocean current $\mathbf{V}'$ (arrows, see scale at top right) and climatological temperature $\overline{T}$ (shading), (b) climatological horizontal ocean current $\overline{\mathbf{V}}$ (arrows, see scale at top right) and anomalous temperature T' (shading), (c) anomalous oceanic upwelling speed w' (contours, interval between solid contours: 10^{-6} m s^{-1}) and climatological vertical temperature stratification $\overline{S}$ (shading), and (d) climatological oceanic upwelling speed $\overline{w}$ (contours, interval: 5×10^{-6} m s^{-1}) and anomalous vertical temperature stratification S' (shading); and of various components of temperature advection: (e) $-\mathbf{V}'\cdot\nabla\overline{T}$, (f) $-\overline{\mathbf{V}}\cdot\nabla T'$, (g) $-w'\overline{S}$, and (h) $-\overline{w}S'$. All results are based on model data for the JAS season. The anomalous fields correspond to the high/warm minus low/cold composites (a) and (b) The $\mathbf{V}$ and T fields are obtained from data at 20-m depth. (c) and (d) The w and S fields are constructed using output at 40-m depth. (e)–(h) The advection terms are computed at 20-m depth. The convention for the color shading in each panel is depicted by a vertical scale bar at the left or right of that panel. (c) and (d) Red, blue, and black contours indicate positive, negative, and zero values, respectively. (c) Dashed red and blue contours correspond to values of $+5 \times 10^{-7}$ and -5×10^{-7} m s^{-1}, respectively.

is offset by the cooling due to climatological upwelling and enhanced temperature stratification in the same region (Figs. 5d and 5h).

The major components of the heat balance in JAS expressed in Eq. (1) are summarized in Fig. 6. The contributions considered here include (a) total horizontal advection, (b) total vertical advection, (c) sum of horizontal and vertical advection, (d) radiative fluxes, (e) heat fluxes, (f) sum of radiative and heat fluxes, and (g) sum of terms in (c) and (f). The patterns in Figs. 6a–c further illustrate the comparable importance of horizontal and vertical advections in lowering the SST in the eastern tropical IO, and the more significant role of horizontal advection in the warming of the western tropical IO.

The pattern for radiative flux anomalies (Fig. 6d) is primarily determined by the shortwave component Q'_{SW}, which is modulated by the amount of cloud cover. Comparison between this chart and those for precipitation data (Figs. 4b and 4e) indicates that the dry anomaly (and, by inference, reduced cloud cover) over the eastern tropical IO is accompanied by enhanced incidence of solar radiation, which leads to oceanic warming. This radiative effect acts to dissipate the cold SST anomaly in the SETIO region associated with the emergent IOP event. The negative feedback between variations in SST and solar heating has also been noted by SAH and Li et al. (2003).

Over the tropical oceans, the anomalous latent heat flux Q'_{LH} is the main contributor to the pattern in Fig. 6e. Q'_{LH} is linked to the local wind speed and specific humidity by the bulk aerodynamic law: higher wind speed and lower humidity increase latent heat loss from the ocean to the atmosphere, thereby cooling the ocean; reduced wind speed and higher humidity would have the opposite effect. These relationships are discernible by comparing the distribution in Fig. 6e with those for wind speed (see Figs. 4a and 4d) and precipitation (which may be regarded as a humidity indicator, see Figs. 4b and 4e).[3] In view of the opposing influences of precipitation anomalies on Q'_{SW} (Fig. 6d) and Q'_{LH} (Fig. 6e), these two terms tend to cancel each other in some locations. The pattern for the total surface radiative and heat flux (Fig. 6f) is characterized by several spatially coherent features in the southern IO. Particularly noteworthy are the cooling tendencies in the central southern IO and off the northwestern Australian coast, as well as the warming in the waters surrounding Madagascar.

The grand total of temperature tendencies due to all advection terms and surface fluxes (Fig. 6g) bears con-

siderable resemblance to the evolution of the SST anomaly pattern from JJA to SON (Figs. 4c and 4f). Comparison among the results in Figs. 6c, 6f, and 6g suggests that temperature advection within the ocean plays a stronger role than surface fluxes in establishing the east–west temperature contrast that is characteristic of the IOP.

b. Temporal evolution

The month-to-month development of selected variables and the heat balance of the top ocean layer are illustrated in Fig. 7. The 12-month period from March of the year when the high/warm and low/cold events occurred [denoted as Year (0)] to February of the following year [denoted as Year (1)] is considered here. A specific month in this period will hereafter be identified by a label consisting of the first three letters of that month, followed by the year indicator in parentheses. The high/warm minus low/cold composites displayed in Fig. 7 include the surface wind vector and wind speed, the vertical ocean current speed at 40-m depth, SST, and precipitation. The individual components of the heat balance of the surface ocean layer (see section 5a) are shown in a cumulative format at the bottom of this figure. Results are presented for spatial averages over three separate sites: (right panels) the SETIO region, (middle panels) the CTIO region, and (left panels) the WTIO region.[4] The locations of these three regions are depicted in Fig. 6g using colored frames.

1) SETIO REGION

Southeasterly surface wind anomalies prevail through the entire period in this region, with peak intensity during the Aug(0)–Oct(0) period (top graph of Fig. 7e). The strongest anomalies in wind speed, oceanic upwelling, and precipitation also occur in this period. Reversal of the direction of the time-mean circulation in this region from southeasterly in northern summer to northwesterly in winter (Lau and Nath 2000; SAH) leads to the weak negative wind speed anomalies in Dec(0)–Feb(1). The coldest SST anomaly appears in Sep(0)–Nov(0).

The evolution of various components of the surface heat budget for this region (Fig. 7f) indicates that $-w'\overline{S}$, $-\overline{\mathbf{V}}\cdot\nabla T'$ and the surface heat fluxes are the main contributors to the cooling tendencies in Jun(0)–Sep(0). These effects are partially offset by radiative warming.

---

[3] Q'_{LH} is also affected by the local oceanic condition: latent heat loss to the atmosphere is enhanced (reduced) above a warm (cold) SST anomaly. This relationship is not apparent from the composite charts for SST (Figs. 4c and 4f) and Q'_{LH} (Fig. 6e), thus indicating that the influences of wind speed and humidity on Q'_{LH} are relatively stronger.

[4] To focus on the evolution of the oceanic upwelling near the east African coast, the vertical current speed for the WTIO region has been obtained by averaging over the smaller area of 10°S–10°N, 40°–50°E. Averages of all atmospheric variables are taken over the entire rectangular sites indicated in Fig. 6g. Averages of SST and all budget terms in the lower panels of Fig. 7 are taken only over the ocean grid points in the IO sector within the individual sites. The model coastlines in the SETIO and WTIO regions are indicated by dashed in Fig. 6g.
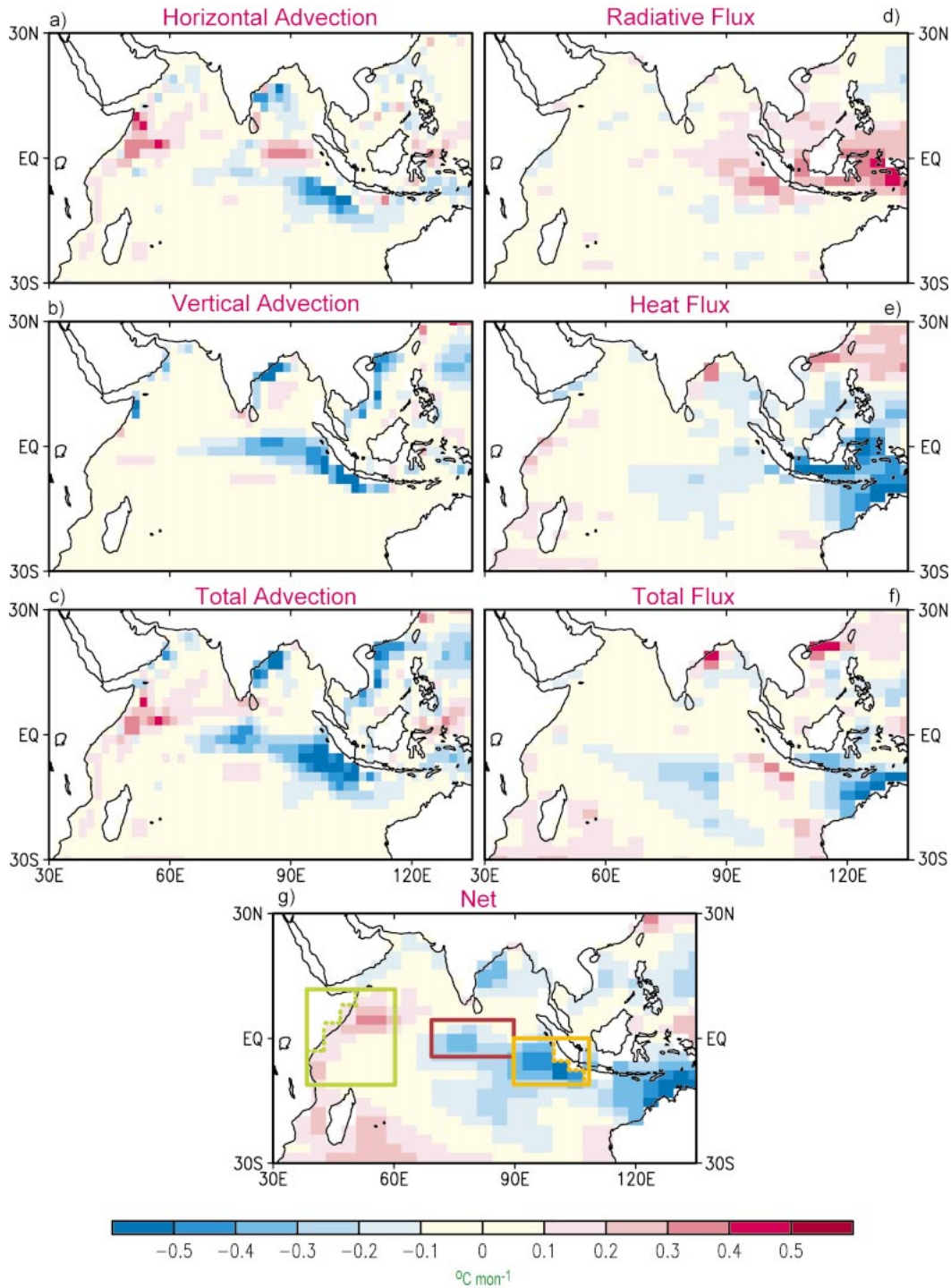
FIG. 6. Distributions of temperature tendency in the top layer of the ocean model during the JAS season due to (a) total horizontal advection $-\mathbf{V}'\cdot\nabla\overline{T} - \overline{\mathbf{V}}\cdot\nabla T'$, (b) total vertical advection $-w'\overline{S} - \overline{w}S'$, (c) total horizontal and vertical advection [sum of (a) and (b)], (d) shortwave and longwave radiative fluxes, (e) latent and sensible heat fluxes, (f) total radiative and heat fluxes [sum of (d) and (e)], and (g) total advection plus total surface fluxes [sum of (c) and (f)]. The convention for the color shading in all panels is indicated by a common scale bar at the bottom of (g). The boundaries of the WTIO, CTIO, and SETIO regions are indicated in (g) using green, red, and orange borders, respectively. The dashed lines within the boxes for WTIO and SETIO indicate the model coastlines in these regions. The sign convention for the surface fluxes is such that positive (negative) fluxes lead to oceanic warming (cooling).
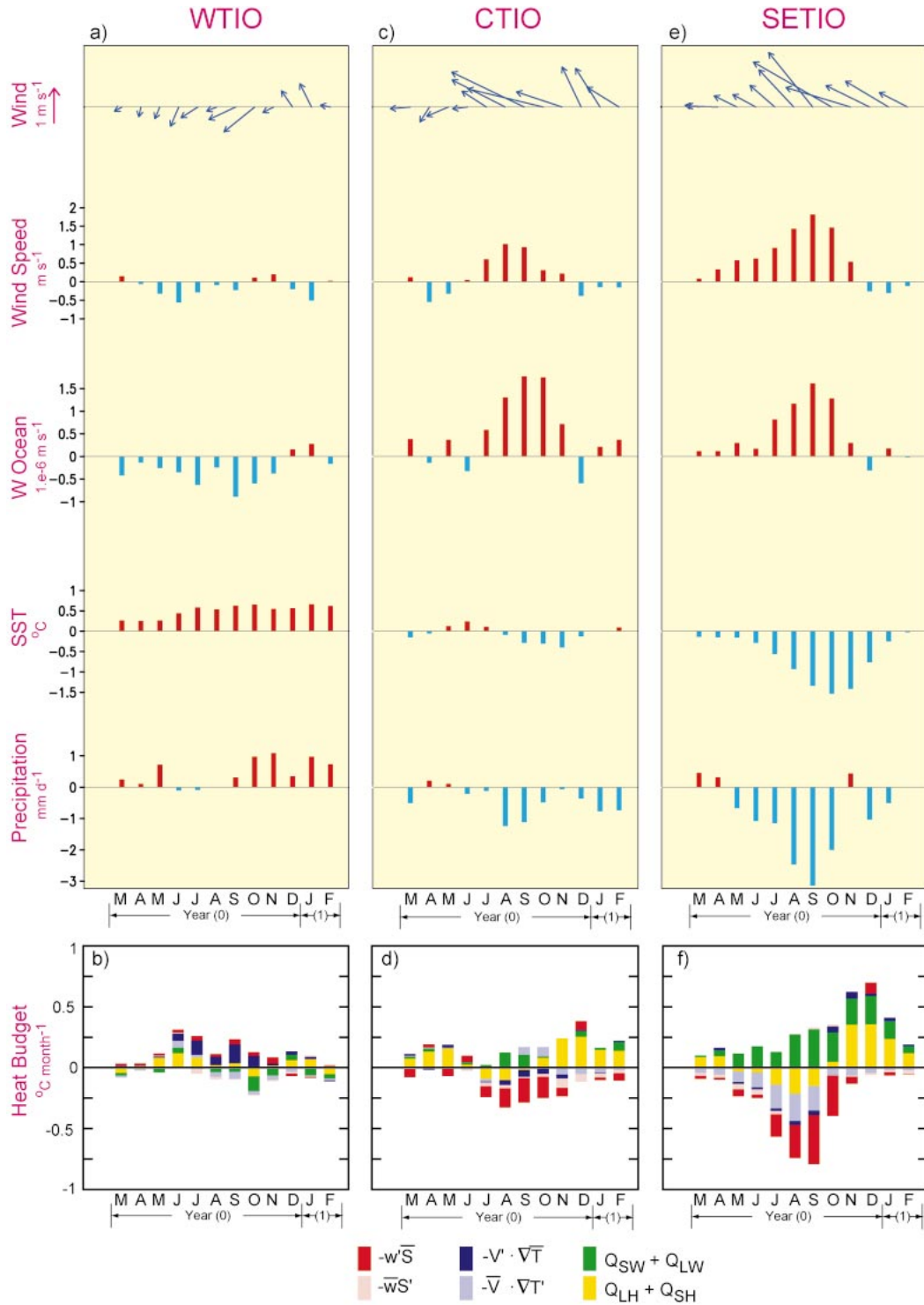
FIG. 7. Temporal evolution of (a), (c), and (e) the anomalous surface wind vector (see scale at extreme left), surface wind speed, oceanic upwelling speed at 40-m depth, SST, and precipitation, and of (b), (d), and (f) various components of the heat budget of the top layer of the ocean model (see legend at bottom), during the 12-month period from Mar of year (0) to Feb of year (1). Results based on averages over the (left) WTIO, (center) CTIO, and (right) SETIO regions (see boundaries depicted in Fig. 6g). (bottom) Contributions to the heat budget by individual processes presented in a cumulative format.

The net temperature tendency becomes positive in Nov(0)–Feb(1), during which the surface heat and radiative fluxes act in concert to warm the surface ocean layer.

The results in Figs. 4, 7e, and 7f delineate the relationships between the surface pressure and wind anomalies in the SETIO region, the modulation of wind speed anomalies due to reversal of the climatological wind direction from northern summer to winter, and the implications of the wind speed changes on the surface heat fluxes and SST development. This chain of processes and their seasonal dependence, as deduced from our model diagnosis, are consistent with the hypothesis put forth earlier by Braak (1919) and further elaborated by Curtis and Hastenrath (1999). The effect of the seasonal reversal in the basic-state atmospheric circulation on local air–sea feedbacks has been incorporated in the conceptual model used by Li et al. (2003) for studying the origin of IOP variability.

2) CTIO REGION

The temporal development of atmosphere–ocean anomalies in this region (Fig. 7c) is similar to that in the SETIO region. The easterly surface wind anomalies during the Aug(0)–Nov(0) period are accompanied by enhanced wind speeds and oceanic upwelling, and by negative changes in the SST and precipitation fields. The SST and precipitation changes are weaker than those in the SETIO region. The results in Fig. 7d illustrate that the cooling tendency in Jul(0)–Oct(0) is primarily due to the $-w'\overline{S}$ term; whereas the heat budget is dominated by the positive temperature changes associated with surface heat flux in Nov(0)–Feb(1).

3) WTIO REGION

The polarity of the changes in this region is mostly opposite to that in SETIO and CTIO. The northeasterly surface wind anomalies during the northern summer and autumn of year (0) are accompanied by weakened wind speed, reduced oceanic upwelling, and SST warming (Fig. 7a). In contrast to the development in SETIO, the strength of the positive SST anomaly in WTIO is almost the same throughout the Jun(0)–Feb(1) period. The most notable enhancement in precipitation is simulated in Oct(0)–Feb(1), several months after the maximum dry anomaly in the eastern portion of the basin. In Jun(0)–Jul(0), almost all of the advective and surface flux terms contribute to oceanic warming (Fig. 7b). During the Aug(0)–Nov(0) period, the processes associated with $-w'\overline{S}$ and $-\mathbf{V}'\cdot\nabla\overline{T}$ continue to raise the SST, whereas the radiative flux leads to oceanic cooling.

The sustained warm SST anomaly in WTIO in the beginning of year (1) (Fig. 7a), and the net positive SST tendencies in SETIO and CTIO during the same period (Figs. 7d and 7f), are consistent with the prevalence of basinwide warming in the IO during the northern winter

and spring of the year after warm ENSO events, as noted by Klein et al. (1999), Goddard and Graham (1999), Lau and Nath (2003), and SAH.

The results of the heat budget analysis presented in this section may be compared with those reported by Murtugudde et al. (2000), Iizuka et al. (2000), Li et al. (2002), SAH, and Shinoda et al. (2003, manuscript submitted to *J. Climate,* hereafter SHA). A majority of these studies noted the contributions of anomalous upwelling, horizontal oceanic transport, and latent heat flux to the SST anomaly in SETIO. These earlier investigations also support our finding on the role of shortwave radiative fluxes in dissipating the SST anomaly in that region during the boreal summer and autumn. Some of the works cited above further indicate the impacts of vertical and horizontal temperature advection as well as oceanic wave propagation on the SST condition in WTIO. There is no clear consensus on the relative importance of oceanic dynamics and surface fluxes in the formation and maintenance of the IOP. Diagnosis of the output from a coupled atmosphere–ocean GCM (Iizuka et al. 2000) and an ocean GCM subjected to observed wind forcing (SHA) indicate that dynamical processes are of primary significance. However, experiments that entail coupling atmospheric GCMs with simple ocean mixed layer models (Baquero-Bernal et al. 2002; SAH) demonstrate that many of the IOP features could be generated using surface flux forcing alone.

6. Occurrence of the IOP in the absence of ENSO events

We now turn our attention to those IOP events that do not coincide with any prominent ENSO development. For this purpose, we have selected four different groups of events satisfying the following criteria based on the IOP index for the SON season and the Niño-4 index for the 6-month period of June–November for the same year:

- IOP index $> +0.75\sigma$; and Niño-4 index has one of the 10 smallest positive values;
- IOP index $> +0.75\sigma$; and Niño-4 index has one of the 10 smallest negative values;
- IOP index $< -0.75\sigma$; and Niño-4 index has one of the 10 smallest positive values; and
- IOP index $< -0.75\sigma$; and Niño-4 index has one of the 10 smallest negative values.

If the above IOP and Niño-4 indices for individual years were plotted in a scattergram similar to that shown in Fig. 3a, the members of the each of the four groups would correspond to those 10 dots that lie closest to the ordinate axis, and are displaced from the abscissa by at least 0.75σ. We shall henceforth merge the first two 10-member groups with IOP $> +0.75\sigma$, and use the label high/weak (i.e., *high* IOP index and *weak* ENSO) to refer to the combined set. Analogously, the last two groups with IOP $< -0.75\sigma$ will collectively be iden-
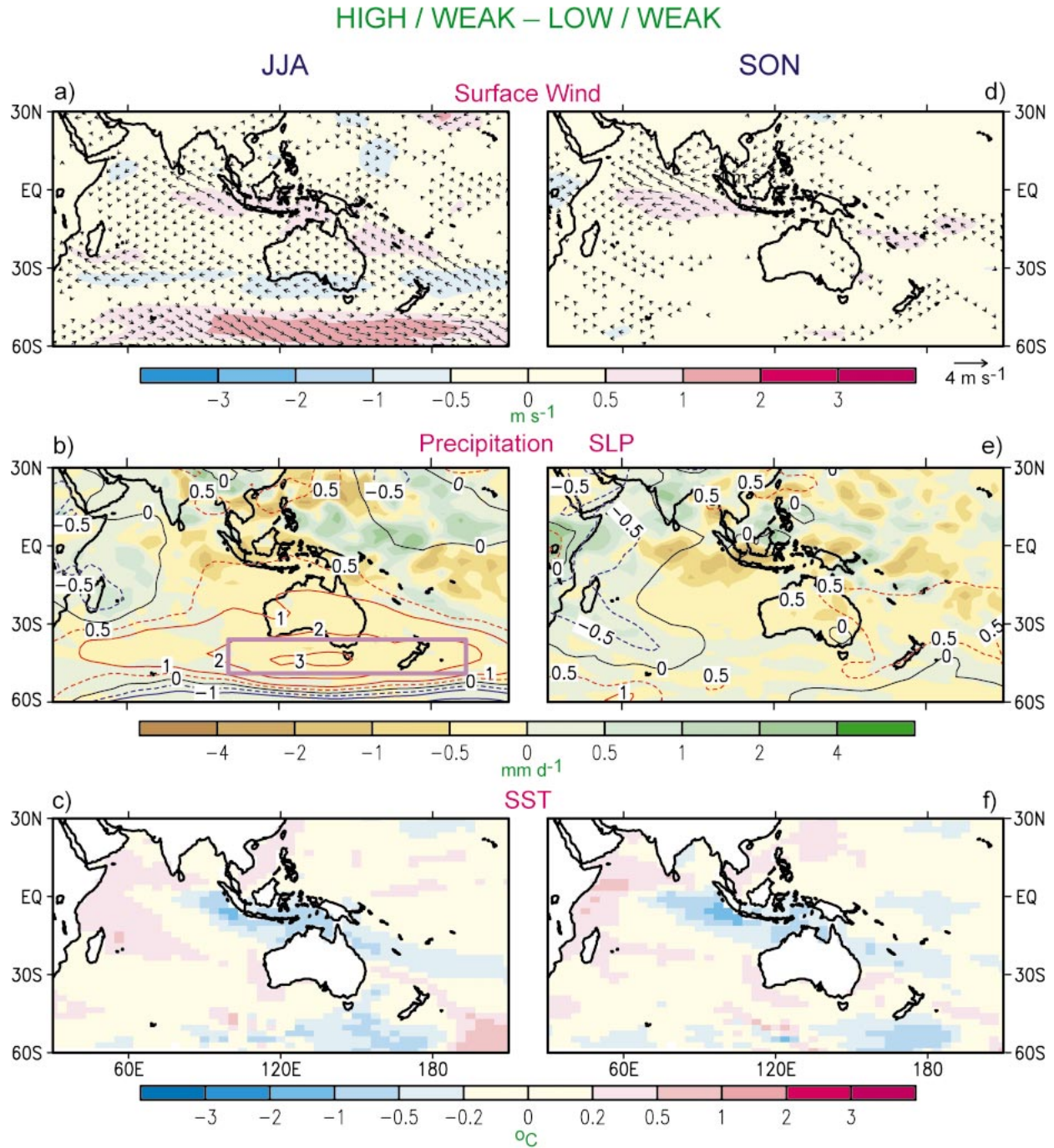
HIGH / WEAK – LOW / WEAK

FIG. 8. As in Fig. 4 except for composite patterns based on differences between the high IOP/weak ENSO and low IOP/weak ENSO cases in the model simulation. (b) The purple rectangular frame indicates the border used in defining the pressure index for the AUS region.

tified as the low/weak set. In forming the high/weak or low/weak sets, the main purpose of incorporating an equal number of weak ENSO events with opposite polarities of the Niño-4 index is to minimize the mean Niño-4 index for each set. Indeed, the cancellations among the positive and negative Niño-4 indices within

the high/weak (low/weak) set result in an averaged Niño-4 index of only -0.05σ $(+0.08\sigma)$.

Composites of selected fields have been calculated for the high/weak and low/weak sets separately. The differences between these two sets of composites (high/weak minus low/weak) are mapped in Fig. 8, for (top

panels) surface wind vector and wind speed, (middle panels) sea level pressure and precipitation, and (bottom panels) SST. Results are shown for the (left panels) JJA and (right panels) SON seasons. The atmospheric and oceanic signals in the equatorial Pacific near the date line in Fig. 8 are uniformly much weaker than those appearing in the high/strong minus low/strong composites (Fig. 4). On the other hand, the characteristic patterns associated with the IOP are clearly present in the tropical IO basin in Fig. 8.

The most striking feature in Fig. 8 is a zonally elongated high pressure anomaly centered at 45°S, with maximum amplitude being simulated south of Australia. We shall henceforth refer to this region as AUS. This anomaly appears in the austral winter (JJA) only (Fig. 8b), and is not discernible in the following season (Fig. 8e). However, some amplification of the wind, precipitation, and SST anomalies in the tropical IO occurs from JJA to SON. It is noteworthy that the pressure change over AUS does not occur in conjunction with strong perturbations of the opposite polarity in the Pacific sector, in sharp contrast to the east–west dipolar pressure pattern accompanying the Southern Oscillation (Figs. 4b and 4e).

Application of the two-tailed Student's t test to the composite values of the pressure field in Fig. 8b indicates that the pressure anomaly in the AUS region is significant at the 95%–99% level. The anomalies of zonal wind in CTIO, as well as those of precipitation and sea level pressure in SETIO and WTIO, are mostly 99% significant in both JJA and SON seasons.

The appearance of the IOP signatures in the high/weak minus low/weak composite suggests that the air–sea interactive processes considered in sections 4–5 could occur within the IO basin even in the near-absence of ENSO forcing from the Pacific. In the high/strong and low/strong episodes, the wind perturbations over the tropical IO are mostly linked to anomalous divergence/convergence associated with precipitation changes over the equatorial Pacific during ENSO (see composite patterns of these fields in Fig. 4). In contrast, the anomalous atmospheric circulation over the tropical IO in the high/weak and low/weak cases (Fig. 8) is primarily associated with in situ air–sea coupling, and possibly also with remote influences of the pressure anomaly over AUS in JJA.

Comparison between the composite patterns for precipitation in Fig. 4 and those in Fig. 8 reveals an interesting difference over much of the Indian subcontinent–Bay of Bengal region. Dryness prevails in this site when positive IOP and warm ENSO events occur simultaneously (Figs. 4b and 4e). The evidence presented by Lau and Nath (2000) and others suggest that this precipitation anomaly is primarily a remote response to ENSO forcing from the tropical Pacific. On the other hand, positive IOP events that occur in the absence of any strong ENSO influences are characterized by above-normal precipitation over the same region (Figs. 8b and

8e). These results suggest that ENSO and IOP could exert rather different influences on the rainfall in the Indian monsoon region.

To further explore the nature of the pressure fluctuations over AUS and their impacts on atmosphere–ocean variability, and to evaluate the fidelity of the model findings, simulated model and observed wind, pressure, and SST fields have been regressed against an index of these pressure changes. This index is defined as the standardized sea level pressure anomaly averaged over the region 35°–50°S, 100°E–165°W, which corresponds to the location of the extremum in the pressure composite pattern in Fig. 8b. The regression patterns thus obtained using JJA data are displayed in Fig. 9.

The pattern in Fig. 9b indicates that simulated pressure variations in the AUS sector are accompanied by changes of the same sign extending along almost the entire latitude circle near 45°S. Poleward of this ring-shaped anomaly is a prominent center over Antarctica with the opposite polarity. The pattern in Fig. 9b is evidently a principal mode of variability in the Southern Hemisphere, since it is very similar to the leading EOF of the pressure field in that region (not shown).[5] The model result also bears a considerable resemblance to its observational counterpart (Fig. 9e) in the Eastern Hemisphere, and to the observed annular structure of the Antarctic Oscillation of the Southern Hemisphere pressure field as documented by Thompson and Wallace (2000) and Limpasuvan and Hartmann (2000). The much stronger pressure changes in the AUS region in the model during southern winter (Fig. 8b) as compared to spring (Fig. 8e) is also consistent with the seasonal dependence of the amplitude of the observed annular mode. The significance of the regression coefficients displayed in Figs. 9b and 9e has been assessed using the two-tailed Student's t test. The ring of positive regression values in Fig. 9b is significant at the 99% level at almost all longitudes along the 30°–50°S zonal belt. The positive feature in Fig. 9e also exceeds the 99% level over much of the midlatitude zone in the Eastern Hemisphere. The negative centers over Antarctica in both the model and observed patterns are also significant at the 99% level.

The regression patterns for the simulated surface wind (Fig. 9a) and SST (Fig. 9c) fields show that positive pressure changes over AUS are coincident with anomalous easterlies and southeasterlies over SETIO and CTIO, and with SST warming (cooling) in WTIO (SETIO). These model relationships are supported by the observational results in Figs. 9d and 9f. As has been previously noted in the discussion of Fig. 1, the simulated positive SST anomaly in WTIO is displaced to the west of the observed location. Significance testing indicates that the easterly anomalies near the SETIO

---

[5] This leading EOF mode explains 25% of the domain-integrated variance. The spatial correlation coefficient between the regression pattern for this leading eigenvector and Fig. 9b is 0.88.
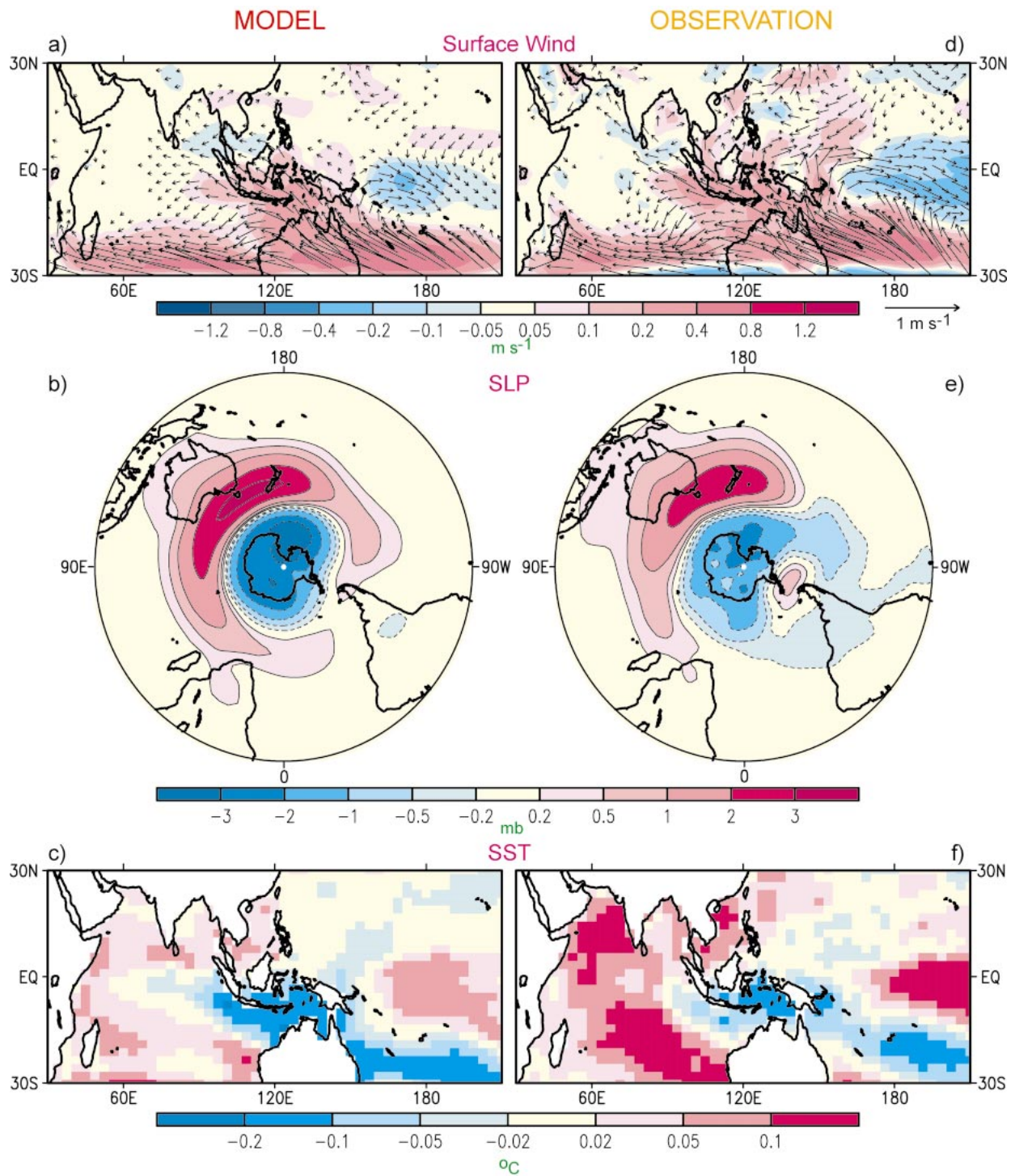
FIG. 9. Distributions of the regression coefficients of (a) and (d) surface wind vector [arrows, see scale below (d)] and wind speed (shading), (b) and (e) sea level pressure, and (c) and (f) SST vs the standardized pressure index for the AUS region (see rectangular boundary in Fig. 8b). Results are shown for the (left) model and (right) observational data for the JJA season. The convention for the color shading in each pair of panels is indicated by a scale bar at the bottom of these panels.
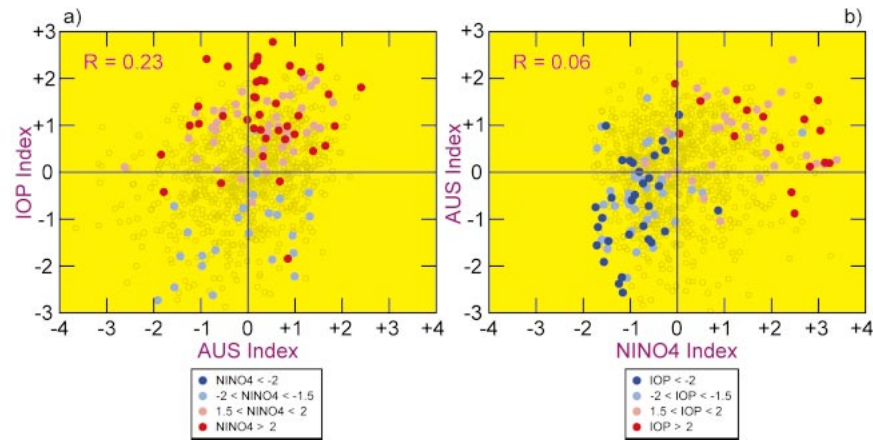
FIG. 10. As in Fig. 3 except for (a) IOP index vs AUS pressure index, and (b) AUS pressure index vs Niño-4 index. Both scattergrams are based on output from the model experiment. (a) The years with Niño-4 indices lying in ranges beyond $\pm 1.5\sigma$ and $\pm 2\sigma$ (see legend box) are indicated by red and blue dots. (b) The years with prominent positive and negative IOP indices are indicated in a similar fashion. The correlation coefficients $R_{\text{IOP,AUS}}$ and $R_{\text{NINO4,AUS}}$ are shown in the upper-left corners of (a) and (b), respectively. The IOP and Niño-4 indices are based on SON data; whereas the AUS index is computed using JJA data (see footnote 6).

region in Figs. 9a surpass the 99% confidence level. The regression values for SST in the model result (Fig. 9c) are 99% significant in SETIO and WTIO; whereas the corresponding observed pattern (Fig. 9f) contain significant (at 90%–95%) anomalies in the central southern IO, Arabian Sea, and the Indonesian waters.

In addition to their possible link with the southern annular mode, the pressure fluctuations in the AUS region may also be related to another prevalent mode of variability referred as the Antarctic Circumpolar Wave by White and Peterson (1996). The pressure and SST perturbations associated with this wave pattern are in spatial quadrature with each other, and are characterized by a wavenumber-two zonal scale and a 3–5-yr period. In their eastward journey along the Southern Ocean, these features could modulate the pressure variability in the AUS region, and thereby influence the development of IOP events. White et al. (2002) noted the presence of positive feedbacks between the Antarctic Circumpolar Wave and ENSO-related phenomena in the Indo-Pacific sector. Further study is evidently needed to delineate the interaction between the atmosphere–ocean anomalies in the Southern Ocean and those in the tropical IO and Pacific.

7. Relationships between IOP, ENSO, and the southern annular mode

The evidence presented in section 4–6 indicates that the IOP is linked to both ENSO events in the tropical Pacific and sea level pressure perturbations over the AUS region. To delineate the covariability among the indices for these three phenomena of interest, scattergrams similar to Fig. 3a are constructed by plotting the IOP index against the AUS index for individual years

in Fig. 10a, and the AUS index against the Niño-4 index in Fig. 10b.[6] Those years corresponding to outstanding warm and cold ENSO events (with absolute value of Niño-4 index exceeding 1.5σ) are depicted in Fig. 10a using red and blue dots, respectively. The years with strong signature of the IOP are marked in Fig. 10b in an analogous manner.

The wider scatter of the data points in Fig. 10a as compared with Fig. 3a indicates that the influence of pressure variations near AUS (and the associated annular mode in the Southern Hemisphere) on the IOP is relatively weaker than the effects of ENSO. This visual impression is confirmed by the lower temporal correlation coefficient between the IOP and AUS indices (denoted as $R_{\text{IOP,AUS}}$, equal to 0.23) than that between IOP and Niño-4 ($R_{\text{IOP,NINO4}}$, equal to 0.55). It should, however, be noted that both correlation values cited here are significant at the 99% level (see footnote 1). Another illustration of the more prominent role of ENSO processes in modulating the SST variability in the tropical IO is the placement of a large majority of the outstanding warm ENSO episodes (red and pink dots) in the upper half of the scatterplot in Fig. 10a (where the IOP index is positive); whereas all the strong cold ENSO events (blue dots) reside in the lower half of the same diagram (with negative IOP index). For those years marked by red and pink dots in the upper left quadrant of Fig. 10a, the impact of warm ENSO is apparently strong enough to yield positive IOP events, in spite of the opposing

---

[6] The IOP and Niño indices displayed in Fig. 10 have been computed using data for the SON season. The AUS index has been computed using JJA data. The calendar season chosen for computing a given index corresponds to the time period when the phenomenon of interest attains peak amplitudes.

influences due to negative pressure changes over AUS. Similarly, the blue dots in the lower right quadrant indicate that the formation of some negative IOP events is attributable to cold ENSO episodes, which more than offset the opposing effects of the concurrent positive AUS pressure anomalies.

The timing of the perturbations associated with ENSO and the southern annular mode relative to IOP events has been further investigated by evaluating correlation coefficients between the Niño-4 and IOP, as well as between AUS and IOP indices at various temporal lags and in various phases of the seasonal cycle. It is seen that the highest $R_{\mathrm{IOP,NINO4}}$ value (0.64) is obtained when Niño-4 in July–August is correlated with IOP in October–November; and that pairing AUS in JJA with IOP in SON yield the maximum $R_{\mathrm{IOP,AUS}}$ (0.23). These results indicate that the ENSO and southern annular model signals tend to precede the IOP phenomena by 2–3 months.

The Niño-4 and AUS indices exhibit a weak relationship with each other (see Fig. 10b), with an insignificant correlation coefficient $R_{\mathrm{NINO4,AUS}}$ of 0.06.[7] The prevalence of strong positive IOP events in the right half of this scattergram (positive Niño-4), and negative IOP events in the left half (negative Niño-4) again signifies the more significant role of ENSO (as compared to pressure changes over AUS) in determining the sign of the IOP.

Since $R_{\mathrm{NINO4,AUS}}$ is negligibly small (0.06), the partial correlation coefficient (e.g., see Panofsky and Brier 1958) between the IOP and ENSO, after discounting the effects of the pressure variations over AUS, is almost the same as $R_{\mathrm{IOP,NINO4}}$. Similarly, the partial correlation between IOP and AUS, after eliminating ENSO influences, is approximately equal to $R_{\mathrm{IOP,AUS}}$. A linear multiple regression analysis of IOP against the variations of the Niño-4 and AUS indices shows that the latter two quantities jointly account for 34% of the variance of IOP, which is close to the sum of the variances explained individually by Niño-4 and AUS (i.e., $R^2_{\mathrm{IOP,NINO4}} + R^2_{\mathrm{IOP,AUS}}$, which equals 36%).

8. Summary and discussion

A recurrent mode of variability of the atmosphere–ocean system in the tropical IO, characterized by east–west contrasts in SST, surface pressure and precipitation, and by marked variations of the surface zonal wind, has been identified in a 900-yr experiment with a coupled GCM. Diagnosis of the model output indicates that the occurrence of these IOP events may be associated with the ENSO phenomenon in the tropical Pacific, and, to a lesser extent, with extratropical sea level pressure fluctuations related to an annular mode in the Southern Hemisphere. It has been demonstrated that both the

ENSO and annular modes modulate the near-surface atmospheric circulation over the equatorial IO. As inferred from an analysis of the surface ocean heat budget, such changes in the wind pattern influence the strength of coastal and open-ocean upwelling, horizontal temperature advection within the top ocean layer, and the amount of latent and sensible heat transfer across the air–sea interface. These processes are conducive to the establishment of an anomalous zonal SST gradient across the equatorial IO. This SST anomaly pattern in turn modifies the overlying atmospheric flow and precipitation pattern. The precipitation anomalies are accompanied by the changes in the cloud cover, which influence the heat balance at the ocean surface by altering the incident solar radiation. Many essential characteristics of the simulated IOP events (e.g., spatial distribution and seasonal dependence of various atmospheric and oceanic anomalies) may be attributed to this chain of processes. The agreement between some of the model findings and observational data suggests that the physical mechanisms considered here are also relevant to the initiation and maintenance of the IOP events in the real atmosphere–ocean system.

The model evidence presented in this study calls for a more balanced perspective on some of the core issues of the current scientific debate on the nature and origin of the IOP events (see section 1). Our results suggest that these events may be linked to multiple causes. Two of these causative factors have been considered here, namely, the ENSO and southern annular modes. Since these two phenomena jointly account for only about one-third of the total variance of the IOP index, it is likely that other modes of variability, such as those related to fluctuations of the Asian–Australian monsoon system and the extratropical flow pattern in the Northern Hemisphere, could also influence air–sea coupling in the IO basin. In addition to the impacts from various types of perturbations located outside of the IO, the feedback mechanisms operating within the IO basin could play a crucial role in the life cycle of the IOP events. For instance, the high/weak minus low/weak composites in Fig. 8 demonstrate that these internal processes are apparently at work in sustaining the IOP anomalies in the SON season, after the cessation of the external influences due to the pressure changes over AUS.

The applicability of the inferences drawn from this study to the IOP events in the observed climate system depends critically on the fidelity of the coupled GCM being examined here. For instance, we have noted that the anomaly center in the simulated SST pattern accompanying ENSO (Fig. 2) is displaced to the west of its observed position. This discrepancy could alter the effectiveness of ENSO in influencing air–sea interaction in the IO basin. However, the model provides a relatively more realistic simulation of the ENSO-related precipitation pattern than the SST pattern [e.g., cf. the model result in Figs. 4b and 4e with its observational

---

[7] The *simultaneous* correlation between the Niño-4 and AUS indices is also weak (0.06 and −0.03 for the JJA and SON seasons, respectively).

counterpart in Fig. 4a of Alexander et al. (2002)]. Since the atmospheric circulation responds more directly to the diabatic heating field, of which the precipitation pattern is a better indicator than the SST pattern, the quality of the ENSO-related wind pattern in the simulation might not be too seriously degraded due to the model errors in reproducing the SST field. Delworth et al. (2002) have noted that this coupled GCM tends to generate ENSO events with longer time scales than observed. This model behavior may have some impact on the temporal evolution and seasonal modulation of the IOP events that are linked to ENSO.

Due to inadequate spatial resolution and model representation of certain processes, the model is limited in its ability to include a variety of mechanisms that may be relevant to the IOP phenomenon. For example, the relatively coarse horizontal resolution of the model could affect the estimation of the strength of coastal upwelling in the SETIO and WTIO regions, as well as the eastward climatological oceanic jets at the equator during the northern autumn (Wyrtki 1973), thereby affecting the accuracy of the $-w'\overline{S}$, $-\overline{w}S'$, and $-\mathbf{V}\cdot\nabla T$ terms in the heat budget of the top ocean layer. Insufficient vertical resolution and the lack of a well-defined oceanic mixed layer or thermocline also lead to difficulties in assessing the role of temperature stratification in air–sea coupling in the IO basin. Other features that need to be more fully incorporated in the model framework are the zonal propagation of oceanic Rossby waves in the tropical IO (e.g., Masumoto and Meyers 1998), and the variability of the Indonesian throughflow (e.g., Meyers 1996; Susanto et al. 2001). Further comparisons with output from experiments conducted independently using other models, and with more detailed observations of various IOP processes, are also needed to validate the findings reported here.

The possible link between the southern annular mode and IOP, as inferred from the results presented in section 6, has thus far received little attention in the research community. Additional model and observational diagnoses are required to ascertain the robustness of this relationship and to delineate its implications on monsoon variability and air–sea coupling in the IO basin. In this context, the secular trend of the southern annular mode, as documented in recent studies by Thompson et al. (2000) and Thompson and Solomon (2002), could be a contributing factor to the changes of the atmosphere–ocean conditions in the tropical IO on decadal time scales.

REFERENCES

Alexander, M. A., I. Bladé, M. Newman, J. R. Lanzante, N.-C. Lau, and J. D. Scott, 2002: The atmospheric bridge: The influence of ENSO teleconnections on air–sea interaction over the global oceans. *J. Climate,* **15,** 2205–2231.

Allan, R. J., and Coauthors, 2001: Is there an Indian Ocean dipole, and is it independent of the El Niño-Southern Oscillation? *CLIVAR Exch.,* **6** (3), 18–22.

——, C. J. C. Reason, J. A. Lindesay, and T. J. Ansell, 2003: 'Protracted' ENSO episodes and their impacts in the Indian Ocean region. *Deep-Sea Res.,* **50B,** 2331–2347.

Baquero-Bernal, A., M. Latif, and S. Legutke, 2002: On the dipolelike variability of sea surface temperature in the tropical Indian Ocean. *J. Climate,* **15,** 1358–1368.

Behera, S. K., and T. Yamagata, 2003: Influence of the Indian Ocean dipole on the Southern Oscillation. *J. Meteor. Soc. Japan,* **81,** 169–177.

——, P. S. Salvekar, and T. Yamagata, 1999: Unusual ocean–atmosphere conditions in the tropical Indian Ocean during 1994. *Geophys. Res. Lett.,* **26,** 3001–3004.

——, S. A. Rao, H. N. Saji, and T. Yamagata, 2003: Comments on "A cautionary note on the interpretation of EOFs." *J. Climate,* **16,** 1087–1093.

Braak, C., 1919: Atmospheric variations of short and long duration in the Malay Archipelago and neighbouring regions, and the possibility to forecast them. Koninklijk Magnetisch en Meteorologisch Observatorium te Batavia, Indonesia, Verhandelingen No. 5, 57 pp.

Chambers, D. P., B. D. Tapley, and R. H. Stewart, 1999: Anomalous warming in the Indian Ocean coincident with El Niño. *J. Geophys. Res.,* **104,** 3035–3047.

Curtis, S., and S. Hastenrath, 1999: Long-term trends and forcing mechanisms of circulation and climate in the equatorial Pacific. *J. Climate,* **12,** 1134–1144.

Delworth, T. L., R. J. Stouffer, K. W. Dixon, M. J. Spelman, T. R. Knutson, A. J. Broccoli, P. J. Kushner, and R. T. Wetherald, 2002: Review of simulations of climate variability and change with the GFDL R30 coupled climate model. *Climate Change,* **19,** 555–574.

Dommenget, D., and M. Latif, 2002: A cautionary note on the interpretation of EOFs. *J. Climate,* **15,** 216–225.

——, and ——, 2003: Reply. *J. Climate,* **16,** 1094–1097.

Enfield, D. B., and A. M. Mestas-Nuñez, 1999: Multiscale variabilities in global sea surface temperatures and their relationships with tropospheric climate patterns. *J. Climate,* **12,** 2719–2733.

Goddard, L., and N. E. Graham, 1999: Importance of the Indian Ocean for simulating rainfall anomalies over eastern and southern Africa. *J. Geophys. Res.,* **104,** 19 099–19 116.

Hanley, D. E., M. A. Bourassa, J. J. O'Brien, S. R. Smith, and E. R. Spade, 2003: A quantitative evaluation of ENSO indices. *J. Climate,* **16,** 1228–1240.

Hastenrath, S., 2002: Dipoles, temperature gradients, and tropical climate anomalies. *Bull. Amer. Meteor. Soc.,* **83,** 735–738.

——, A. Nicklis, and L. Greischar, 1993: Atmospheric–hydrospheric mechanisms of climate anomalies in the western equatorial Indian Ocean. *J. Geophys. Res.,* **98,** 20 219–20 235.

Huang, B., and J. L. Kinter III, 2002: Interannual variability in the tropical Indian Ocean. *J. Geophys. Res.,* **107,** 3199, doi:10.1029/2001JC001278.

Iizuka, S., T. Matsuura, and T. Yamagata, 2000: The Indian Ocean SST dipole simulated in a coupled general circulation model. *Geophys. Res. Lett.,* **27,** 3369–3372.

Kalnay, E., and Coauthors, 1996: The NCEP/NCAR 40-Year Reanalysis Project. *Bull. Amer. Meteor. Soc.,* **77,** 437–471.

Kawamura, R., 1998: A possible mechanism of the Asian summer monsoon–ENSO coupling. *J. Meteor. Soc. Japan,* **76,** 1009–1027.

Klein, S. A., B. J. Soden, and N.-C. Lau, 1999: Remote sea surface

temperature variations during ENSO: Evidence for a tropical atmospheric bridge. *J. Climate,* **12,** 917–932.

Knutson, T. R., and S. Manabe, 1998: Model assessment of decadal variability and trends in the tropical Pacific Ocean. *J. Climate,* **11,** 2273–2296.

Krishnamurthy, V., and B. P. Kirtman, 2003: Variability of the Indian Ocean: Relation to monsoon and ENSO. *Quart. J. Roy. Meteor. Soc.,* **129,** 1623–1646.

Lau, N.-C., and M. J. Nath, 1996: The role of the ''atmospheric bridge'' in linking tropical Pacific ENSO events to extratropical SST anomalies. *J. Climate,* **9,** 2036–2057.

——, and ——, 2000: Impact of ENSO on the variability of the Asian–Australian monsoons as simulated in GCM experiments. *J. Climate,* **13,** 4287–4309.

——, and ——, 2003: Atmosphere–ocean variations in the Indo-Pacific sector during ENSO episodes. *J. Climate,* **16,** 3–20.

Li, T., Y. Zhang, E. Lu, and D. Wang, 2002: Relative role of dynamic and thermodynamic processes in the development of the Indian Ocean dipole: An OGCM diagnosis. *Geophys. Res. Lett.,* **29,** 2110, doi:10.1029/2002GL015789.

——, B. Wang, C.-P. Chang, and Y. Zhang, 2003: A theory for the Indian Ocean dipole–zonal mode. *J. Atmos. Sci.,* **60,** 2119–2135.

Limpasuvan, V., and D. L. Hartmann, 2000: Wave-maintained annular modes of climate variability. *J. Climate,* **13,** 4414–4429.

Loschnigg, J., G. A. Meehl, P. J. Webster, J. M. Arblaster, and G. P. Compo, 2003: The Asian monsoon, the tropospheric biennial oscillation, and the Indian Ocean zonal mode in the NCAR CSM. *J. Climate,* **16,** 1617–1642.

Masumoto, Y., and G. Meyers, 1998: Forced Rossby waves in the southern tropical Indian Ocean. *J. Geophys. Res.,* **103,** 27 589–27 602.

Meyers, G., 1996: Variation of Indonesian throughflow and the El Niño–Southern Oscillation. *J. Geophys. Res.,* **101,** 12 255–12 263.

Murtugudde, R., J. P. McCreary, and A. J. Busalacchi, 2000: Oceanic processes associated with anomalous events in the Indian Ocean with relevance to 1997–1998. *J. Geophys. Res.,* **105,** 3295–3306.

Nicholls, N., 1995: All-India summer monsoon rainfall and sea surface temperature around northern Australia and Indonesia. *J. Climate,* **8,** 1463–1467.

Pacanowski, R., K. Dixon, and A. Rosati, 1991: The GFDL modular ocean model users guide version 1. GFDL Ocean Group Tech. Rep. 2, 44 pp. [Available from GFDL/NOAA, Princeton University, P. O. Box 308, Princeton, NJ 08542.]

Panofsky, H. A., and G. W. Brier, 1958: *Some Applications of Statistics to Meteorology.* The Pennsylvania State University, 224 pp.

Rao, S. A., S. K. Behera, Y. Masumoto, and T. Yamagata, 2002: Interannual subsurface variability in the tropical Indian Ocean with a special emphasis on the Indian Ocean dipole. *Deep-Sea Res.,* **49B,** 1549–1572.

Reason, C. J. C., R. J. Allan, J. A. Lindesay, and T. J. Ansell, 2000: ENSO and climatic signals across the Indian Ocean Basin in the global context: Part 1, Interannual composite patterns. *Int. J. Climatol.,* **20,** 1285–1327.

Saji, N. H., and T. Yamagata, 2003: Structure of SST and surface wind variability during Indian Ocean Dipole Mode events: COADS observations. *J. Climate,* **16,** 2735–2751.

——, B. N. Goswami, P. N. Vinayachandran, and T. Yamagata, 1999: A dipole mode in the tropical Indian Ocean. *Nature,* **401,** 360–363.

Schopf, P. S., and M. J. Suarez, 1988: Vacillations in a coupled ocean–atmosphere model. *J. Atmos. Sci.,* **45,** 549–566.

Shinoda, T., M. A. Alexander, and H. H. Hendon, 2004: Remote

response of the Indian Ocean to interannual SST variations in the tropical Pacific. *J. Climate,* **17,** 362–372.

Shukla, J., 1987: Interannual variability of monsoon. *Monsoons,* J. S. Fein and P. L. Stephens, Eds., Wiley, 399–464.

Smith, T. M., R. W. Reynolds, R. E. Livezey, and D. C. Stokes, 1996: Reconstruction of historical sea surface temperatures using empirical orthogonal functions. *J. Climate,* **9,** 1403–1420.

Susanto, R. D., A. L. Gordon, and Q. Zheng, 2001: Upwelling along the coasts of Java and Sumatra and its relation to ENSO. *Geophys. Res. Lett.,* **28,** 1599–1602.

Thompson, D. W. J., and J. M. Wallace, 2000: Annular modes in the extratropical circulation. Part I: Month-to-month variability. *J. Climate,* **13,** 1000–1016.

——, and S. Solomon, 2002: Interpretation of recent Southern Hemisphere climate change. *Science,* **296,** 895–899.

——, J. M. Wallace, and G. C. Hegerl, 2000: Annular modes in the extratropical circulation. Part II: Trends. *J. Climate,* **13,** 1018–1036.

Tourre, Y. M., and W. B. White, 1995: ENSO signals in global upper-ocean temperature. *J. Phys. Oceanogr.,* **25,** 1317–1332.

——, and ——, 1997: Evolution of the ENSO signal over the Indo-Pacific domain. *J. Phys. Oceanogr.,* **27,** 683–696.

——, B. Rajagopalan, Y. Kushnir, M. Barlow, and W. B. White, 2001: Patterns of coherent decadal and interdecadal climate signals in the Pacific basin during the 20th century. *Geophys. Res. Lett.,* **28,** 2069–2072.

Trenberth, K. E., and D. P. Stepaniak, 2001: Indices of El Niño evolution. *J. Climate,* **14,** 1697–1701.

Vinayachandran, P. N., S. Iizuka, and T. Yamagata, 2002: Indian Ocean dipole mode events in an ocean general circulation model. *Deep-Sea Res.,* **49B,** 1573–1596.

Wallace, J. M., E. M. Rasmusson, T. P. Mitchell, V. E. Kousky, E. S. Sarachik, and H. von Storch, 1998: On the structure and evolution of ENSO-related climate variability in the tropical Pacific: Lessons from TOGA. *J. Geophys. Res.,* **103,** 14 241–14 260.

Wang, B., R. Wu, and T. Li, 2003: Atmosphere–warm ocean interaction and its impacts on the Asian–Australian monsoon variation. *J. Climate,* **16,** 1195–1211.

Weare, B. C., 1979: A statistical study of the relationship between ocean surface temperatures and the Indian monsoon. *J. Atmos. Sci.,* **36,** 2279–2291.

Webster, P. J., A. M. Moore, J. P. Loschnigg, and R. R. Leben, 1999: Coupled ocean–atmosphere dynamics in the Indian Ocean during 1997–98. *Nature,* **401,** 356–360.

White, W. B., and R. Peterson, 1996: An Antarctic Circumpolar Wave in surface pressure, wind, temperature, and sea ice extent. *Nature,* **380,** 699–702.

——, and R. J. Allan, 2001: A global quasi-biennial wave in surface temperature and pressure and its decadal modulation from 1900 to 1994. *J. Geophys. Res.,* **106,** 26 789–26 804.

——, S.-C. Chen, R. J. Allan, and R. C. Stone, 2002: Positive feedbacks between the Antarctic Circumpolar Wave and the global El Niño–Southern Oscillation wave. *J. Geophys. Res.,* **107,** 3165, doi:10.1029/2000JC000581.

Wyrtki, K., 1973: An equatorial jet in the Indian Ocean. *Science,* **181,** 262–264.

Xie, S.-P., H. Annamalai, F. A. Schott, and J. P. McCreary, 2002: Structure and mechanisms of South Indian Ocean climate variability. *J. Climate,* **15,** 864–878.

Yamagata, T., S. K. Behera, S. A. Rao, Z. Guan, K. Ashok, and H. N. Saji, 2002: The Indian Ocean dipole: A physical entity. *CLIVAR Exch.,* **7** (2), 15–18.

Yu, L.-S., and M. M. Reinecker, 1999: Mechanisms for the Indian Ocean warming during the 1997–98 El Niño. *Geophys. Res. Lett.,* **26,** 735–738.